The Impact of GIA Corrections on Gravimetric Basin-Scale Ocean Mass Budgets

En-Chi Lee[1,2] and Christopher Harig[1]

[1]Department of Geosciences, University of Arizona
[2]Lunar and Planetary Laboratory, University of Arizona

Peer review status:
This is a non-peer-reviewed preprint submitted to EarthArXiv.

Key Points:

- We provide joint sea-level budget estimates from GRACE/GFO gravimetry, altimetry-steric, and fingerprint methods over the 2003–2022 period using 32 different glacial isostatic adjustment (GIA) models, along with rederived geocentric motion consistent with each GIA correction.
- The basin-scale ocean mass budget non-closure is significantly affected by the choice of GIA model, directly and indirectly through the geocentric motion estimates.
- The long wavelength agreement between GRACE and altimetry prefers GIA models with less LGM ice load in Antarctica and more load or later deglaciation in Fennoscandia.

Corresponding author: En-Chi Lee, `williameclee@arizona.edu`

Abstract

Closing the sea-level budget is crucial for validating our understanding of climate change and sea-level rise. Satellite gravimetry (Gravity Recovery and Climate Experiment, GRACE) and altimetry are primary tools for measuring the ocean mass. Still, both datasets must be corrected for glacial isostatic adjustment (GIA), the ongoing viscoelastic response of the Earth to past deglaciation. Disagreements amongst GIA models, from ice histories to Earth rheological structures, create uncertainties not captured by many previous studies, especially at ocean basin scales. Using an ensemble of 32 GIA models, we show that whilst the global ocean mass budget closes (at 2.25 ± 0.48 mm/yr from GRACE and 2.28 ± 0.16 mm/yr from altimetry-steric), the choice of GIA model is the dominant driver of non-closure at basin scales. These discrepancies are strongest in the long-wavelength coefficients that can arise directly from the GIA rotational response and indirectly through the GIA-corrected geocentric motion estimates. They manifest differently in gravimetric, altimetric, and sea-level fingerprint (SLF) estimates. No single GIA model can simultaneously close the mass budget in all basins, demonstrating that closing the basin-scale ocean mass budget provides a powerful new and independent constraint for GIA model development. Our results suggest that reconciling basin-scale sea level observations favours a GIA model with a stronger response in the Northern Hemisphere, potentially from a larger or later-deglaciating Fennoscandian Ice Sheet. Such findings provide a path to resolving GIA model ambiguity and improving regional sea level change projections.

Plain Language Summary

Sea level changes over the past two to three decades rely heavily on satellite gravimetry and altimetry. Nonetheless, estimates from these two techniques often disagree, especially at ocean basin scales. A commonly underestimated source of uncertainty in these estimates is the correction for glacial isostatic adjustment (GIA), the ongoing response of the solid Earth to past ice melt. Different GIA models, based on various assumptions about past ice melt and Earth's structure, can yield significantly different corrections. Using 32 different GIA models to correct ocean mass estimates from gravimetry, altimetry, and sea level fingerprints, we show that the choice of GIA model is a dominant source of discrepancy in closing the ocean mass budget at basin scales. Based on the patterns of disagreement, we further suggest that GIA models with more ice or later deglaciation in Fennoscandia during the last ice age and less ice in Antarctica are preferred.

1 Introduction

Understanding contemporary sea level change is crucial for future climate projections and coastal planning. A key validation of our understanding of sea level change is the closure of the sea-level budget, that is, the agreement between the observed sea level change and the sum of the contributing processes. The global mean sea-level budget has been measured to high precision over the past two decades (WCRP Global Sea Level Budget Group, 2018; Chen et al., 2019) using the latest satellite gravimetry missions Gravity Recovery and Climate Experiment (GRACE)/GRACE Follow-On (GFO), the Jason-1–3 altimetry missions, and in-situ ocean measurements including the Argo float network. With these advancements, the increase in ocean mass resulting from land ice melt and changes in terrestrial water storage has been identified as the dominant contributor to global mean sea level rise in recent years (Fox-Kemper et al., 2021; Ludwigsen et al., 2024).

While global ocean mass change is relatively well constrained, it is not spatially uniform, and closing the sea-level budget at ocean-basin scales remains challenging. The regional patterns of ocean mass are affected by many processes, including atmospheric and oceanic dynamics and thermodynamics, the sea-level fingerprint (SLF) of the self-attraction and loading effect of mass redistribution, and the Earth's ongoing viscoelastic response to past ice sheet and glacier melt, a process known as glacial isostatic adjustment (GIA) (Tamisiea, 2011; Adhikari et al., 2019; Vishwakarma et al., 2020). The difficulty in accurately disentangling signals from these contributors with finer spatial details leads to significant discrepancies in basin-scale ocean mass estimates, depending on the data and processing methods used (e.g. Rietbroek et al., 2016; Jeon et al., 2021; Ludwigsen et al., 2024). The non-closure challenges the current understanding of sea level change processes.

A potentially overlooked source of such disagreement in regional ocean mass and sea-level budgets is the GIA effect. GIA models are used to correct satellite gravimetry and altimetry observations for the secular signals of solid Earth deformation, which are unrelated to modern surface mass redistribution (e.g. Caron et al., 2018; Peltier et al., 2018). The correction can significantly modify regional ocean mass trends, but gravimetry and altimetry observations are affected by GIA in different ways. This implies that an unsatisfactory GIA correction can either introduce or mask discrepancies in ocean mass budgets. The GIA correction is particularly significant for gravimetry (i.e. GRACE/GFO geoid measurements), where its magnitude can be comparable to the modern ocean mass change in some ocean basins. Furthermore, GIA has a substantial influence on the GRACE-based estimate of the geocentric motion, which, in turn, strongly affects the estimated water mass partitioning between the Northern and Southern Hemispheres. The resemblance between the spatial patterns of GIA corrections and the long-wavelength discrepancies observed between altimetry-steric and gravimetry-based ocean mass estimates (e.g. Mu et al., 2024) strongly suggests that uncertainties amongst GIA models may be a key contributor to the non-closure of regional sea-level budgets.

Accurate GIA modelling is taxing, primarily due to incomplete knowledge of the past ice-load history since the Last Glacial Maximum (LGM) and of Earth's viscoelastic structure, the two key ingredients in GIA models. A notable uncertainty amongst different ice history models is the amount of global ice load during LGM, known as the 'missing ice problem' (Simms et al., 2019; Peltier et al., 2022). For instance, with a lack of near-field constraints in Antarctica, some ice history models place significantly more ice on the continent than others (cf. Lambeck et al., 2014; Peltier et al., 2018), leading to very different GIA predictions in the Southern Ocean and beyond. Moreover, GIA models are typically constrained by terrestrial data and incorporate virtually no data from the open ocean into their construction, leaving their applicability for ocean mass correction an open question. Quantifying the uncertainty in GIA models and their effects on ocean mass estimates is therefore crucial for understanding modern ocean mass change whilst providing feedback to improve GIA models.

Despite the significant differences amongst GIA model predictions, most studies on ocean mass change rely on a single model, or a very small number of models, to correct for the GIA effect. This over-reliance on a single model can lead to biased results and hinder inter-study comparability, ultimately impeding progress in understanding sea level change. To address this problem, this study investigates the impact of GIA inter-model uncertainty on the closure of the ocean mass budget at global and basin scales (as defined in Figure 1(f)). We use a suite of 32 different GIA models to correct for ocean mass estimates derived from three different methods: the GRACE-based gravimetric estimate, the altimetry-steric estimate, and the forward modelling of SLFs plus ocean dynamics. By comparing the results from these three approaches, we aim to identify which GIA models are most consistent with the observational record and provide a more robust assessment of the uncertainties in regional ocean mass change. These findings in turn constrain GIA models. Section 2 reviews the theoretical background of the GIA-corrected ocean mass budget and the three different methods used in this study, and Section 3 describes the data used and additional processing steps. Sections 4 and 5 discuss different GIA models' ability to close basin-scale mass budgets and the implications of the ice history models.

2 The GIA-Corrected Ocean Mass Budget

The total relative sea level (RSL) change Δs is defined as the change in the difference between the sea surface h and ocean bottom height r. We decompose it into four main components, including (1) the modern water redistribution from the land-ocean mass exchange (the SLF, Δs^{SLF}), (2) oceanic and atmospheric dynamics ($\Delta s^{\mathrm{dynamics}}$),

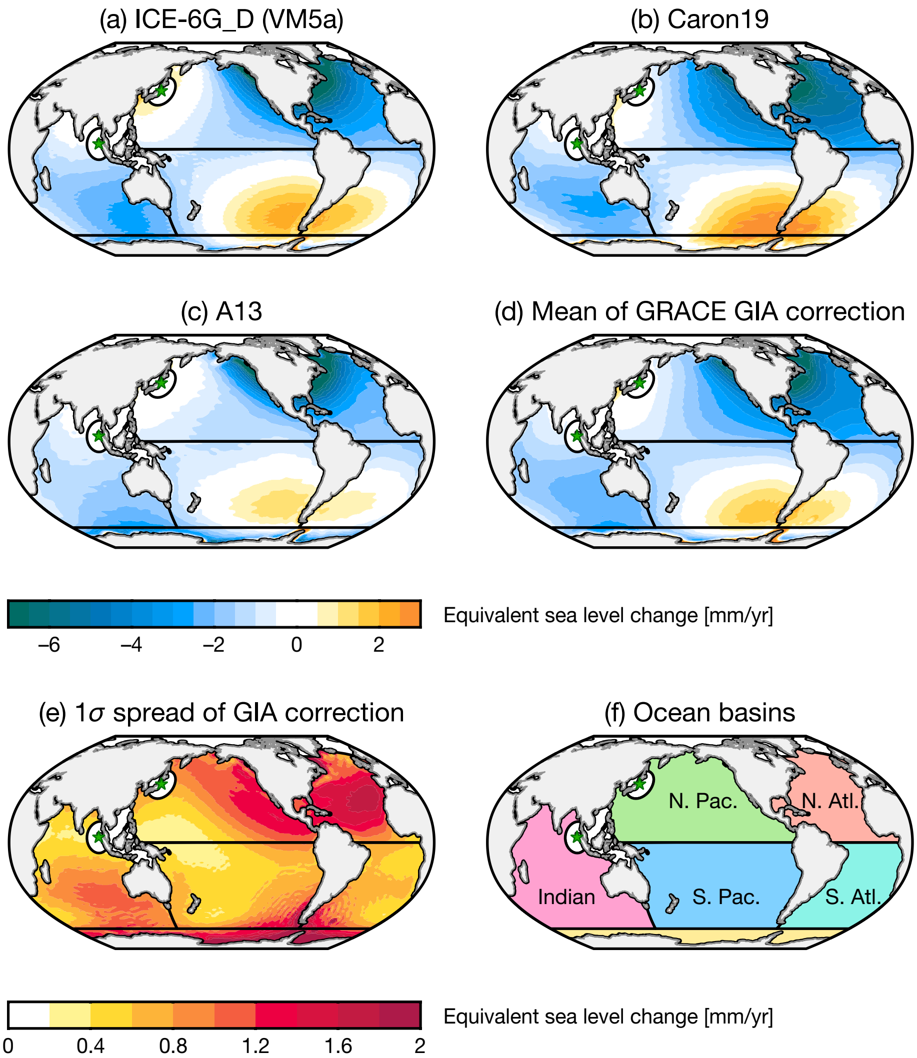

Figure 1: Magnitude of GIA corrections applied to the GRACE/GFO mass trend estimates according to different models, converted to equivalent water thickness and truncated to spherical harmonic d/o 60, from (a) to (c): ICE-6G_D (VM5a) (Peltier et al., 2018), Caron19 (Caron & Ivins, 2020), and A13 (A et al., 2013). (d) and (e) show the ensemble mean and one standard deviation spread of all GIA models used in this study (see Table 1). Also shown in (f) is the division of the ocean basins used in this study. Areas around two large coastal megathrust earthquakes, denoted by stars, are removed (see Section 3.4).

(3) the viscoelastic response of the Earth due to past ice sheet deglaciation (Δs^{GIA}), and (4) the steric sea level anomaly ($\Delta s^{\mathrm{steric}}$) (e.g. Tamisiea, 2011; Jeon et al., 2021) as:

$$\Delta s = \Delta h - \Delta r = \Delta s^{\mathrm{SLF}} + \Delta s^{\mathrm{dynamics}} + \Delta s^{\mathrm{GIA}} + \Delta s^{\mathrm{steric}} + \epsilon. \tag{1}$$

Other unaccounted changes, most notably megathrust earthquakes and errors, are represented by ϵ. Changes in h and r can be decomposed in the same way.

When studying modern processes, it is conventional to consider the 'GIA-corrected' sea level $\Delta s'(\omega, t)$ or ocean mass that removes the contribution of GIA as (Mu et al. 2025; Spada 2017, Equations (49) and (53))

$$\Delta s' = \Delta s - \Delta s^{\mathrm{GIA}}, \tag{2}$$

where all terms are functions of a point ω on a sphere (defined by colatitude θ and longitude ϕ coordinates) and time t. The change in surface density associated with the modern water redistribution is found by including the mean water density ρ_{w} as

$$\Delta L' = \rho_{\mathrm{w}}(\Delta s' - \Delta s^{\mathrm{steric}}) = \rho_{\mathrm{w}}(\Delta s^{\mathrm{SLF}} + \Delta s^{\mathrm{dynamics}} + \epsilon). \tag{3}$$

Since $\Delta s^{\mathrm{steric}}$ creates no net mass change, it does not contribute to the load to the first order. The GIA-corrected mass change $\Delta M'$ in an ocean basin is then found by integration over the basin, on the unit sphere Ω, as

$$\Delta M'(t) = \int_{\mathrm{basin}} \Delta L'(\omega, t)\, \mathrm{d}\Omega\,. \tag{4}$$

We examine the ocean basin mass budget obtained in three different ways. First, given the RSL change obtained through altimetry and the steric sea level from e.g. Jason and Argo (Ludwigsen et al., 2024), the load can be estimated by rearranging Equation 3. Second, the surface mass density change can be inverted from the geoid anomaly change, assuming such an anomaly is indeed induced by the surface water load. Finally, the load can also be forward modelled by solving the sea level equation (SLE) with a given forcing for the fingerprint component Δs^{SLF}.

2.1 Gravimetric Mass Change

GRACE measures geoid perturbations, and the height changes Δn can be transformed into surface density changes in the spherical harmonic domain as in Wahr et al.

(1998) via

$$\Delta n_{\ell m} = \frac{3}{\rho_\oplus}\frac{1+k_\ell^{\mathrm{E}}}{2\ell+1}\Delta L_{\ell m}, \tag{5}$$

where ℓ and m are the spherical harmonic degree and order, respectively. Here, $\rho_\oplus$ is the mean density of the Earth and k_ℓ^{E} is the elastic load Love number for geoid height at spherical harmonic degree ℓ. Not all geoid perturbation is induced by modern surficial water mass redistribution; GIA signals are also strong in the geoid field. Hence, a GIA correction is applied to the geoid height before being used in Equation 5:

$$\Delta n' = \Delta n - \Delta n^{\mathrm{GIA}}. \tag{6}$$

2.2 Steric-Corrected Altimetry Mass Change

Altimetry measurements of the sea surface height h are also corrected for the GIA contribution, similar to Equation 6 (Tamisiea, 2011). The difference is that, under the static equilibrium assumption, the GIA sea surface differs from the geoid perturbation n by some spatially uniform constant $\bar{n}$ such that

$$\Delta h' = \Delta h - (\Delta n^{\mathrm{GIA}} + \Delta \bar{n}^{\mathrm{GIA}}). \tag{7}$$

In the case where $\Delta \bar{n}^{\mathrm{GIA}}$ is not known, it can be found by enforcing the conservation of water mass (Tamisiea, 2011, Figure 4) by

$$0 = \int_{\text{ocean}} (\Delta n^{\mathrm{GIA}}(\omega) + \Delta \bar{n}^{\mathrm{GIA}} - \Delta r^{\mathrm{GIA}}(\omega))\,\mathrm{d}\Omega, \tag{8}$$

where r^{GIA} is the GIA-induced vertical land motion.

To obtain the RSL and consequently the ocean mass, the steric sea level and the modern load-induced ocean bottom deformation (OBD) are also removed. The latter can be estimated from an independently measured load, which, in this study, is from GRACE's geoid perturbation in the spherical harmonics space $\Delta n'_{\ell,m}$ (Vishwakarma et al., 2020):

$$\Delta r'_{\ell,m} = \frac{f_\ell^{\mathrm{E}}}{1+k_\ell^{\mathrm{E}}}\Delta n'_{\ell,m}. \tag{9}$$

Here f_ℓ^{E} is the elastic load Love number for vertical land motion.

2.3 Sea-Level Equation

We estimate the ocean mass change by solving the fingerprint of the modern terrestrial water storage change with the SLE. At regional to coastal scales, sea level reconstructed with the SLE shows better agreement with altimetry than the mascon solution (Jeon et al., 2018). Since we are solving for decadal-scale basin mass, a fixed-coastline elastic SLE including rotational feedback is used, as described in Adhikari et al. (2019) and outlined in the Supporting Information. The coastline is assumed to be fixed, and the modern ocean load is deemed small enough that its viscous response is negligible. The forcing is estimated from the GRACE mass change using the same method as described in Section 2.1, with no filtering or rescaling applied.

3 Data and Methods

3.1 Satellite and Model Products

We use the GRACE and GFO Level-2 monthly degree/order (d/o) 60 geopotential spherical harmonics coefficient products from the three product centres of Center for Space Research (CSR), Jet Propulsion Laboratory (JPL), and GFZ Helmholtz-Zentrum für Geoforschung (GFZ) (Release 6.3), mainly between January 2003 and December 2022. The d/o 96 products are not used in this study because we found that the higher-degree coefficients contain too much noise and yield non-realistic estimates compared to the results from d/o 60 products and altimetry-steric estimates. By default, the degree-1 coefficients (ΔC_{10}, ΔC_{11}, and ΔS_{11}) are replaced with the solutions from Technical Note (TN)-13 (Sun, Riva, & Ditmar, 2016), and ΔC_{20} and ΔC_{30} are replaced with the satellite laser ranging (SLR)-derived values in TN-14 (Loomis et al., 2020), when available. The degree-1 coefficients are further modified to account for potential GIA model biases (see Section 3.2). The monthly atmosphere-ocean model product ('GAD') is also restored (Uebbing et al., 2019; Vishwakarma et al., 2020).

For the altimetry-steric time series, we use sea surface height anomaly data from the Making Earth System Data Records for Use in Research Environments (MEaSUREs) programme, which compiles data from various altimetry missions and applies the wet troposphere correction. The seawater temperature and salinity data are obtained from the ensemble of two datasets, including the Scripps Institution of Oceanography (SIO) Argo network (Roemmich & Gilson, 2009) and UK Met Office's multi-mission EN4.2.2.c14 model, which adopts bias correction from L. Cheng et al. (2014). The steric sea level anomaly is subsequently computed following the published code for the Heat and Ocean Mass from Gravity ESDR (HOMaGE) project (`https://github.com/podaac/HOMaGE`), using the Thermodynamic Equation Of Seawater - 2010 (TEOS-10) (McDougall & Barker, 2011). The global mean halosteric sea level is removed to account for the salinity drift in the Argo data (e.g. Mu et al., 2024).

We examine 32 different global GIA models in this study (Table 1). These include the ICE-6G_D (VM5a) model (Peltier et al., 2018, hereafter abbreviated to 'ICE-6G'), and models from Caron et al. (2018); Caron & Ivins (2020), which together are arguably the most recent and widely used global GIA models currently. The A et al. (2013) and Paulson et al. (2007) models are also included for comparison, as they have been widely used in the glaciology and oceanography communities (Chen et al., 2018; Uebbing et al., 2019; Shepherd et al., 2019, see also references therein).

Steffen (2021) and LM17.3 (Steffen et al., 2021) are 27 additional models that are derived from the combinations of different Earth profiles and ice histories, including and not limited to the ICE-6G_C, ICE-7G_NA, and ANU-ICE ice models, and VM5a, VM7, and various 2-layer viscosity profiles (Peltier et al., 2018; Lambeck et al., 2014). This collection of models, although given less weight in the ensemble, represents the broader uncertainty in the GIA correction and the sensitivity to GIA model selection.

Model code	Source	Notes
A13	A et al. (2013)	Laterally varying Earth model.
Caron18	Caron et al. (2018)	
Caron19	Caron & Ivins (2020)	Similar to Caron18; optimised for the Antarctica.
Paulson07	Paulson et al. (2007)	Modified from ICE-5G.
ICE-6G	Peltier et al. (2018)	Earth profile from VM5a; ice history from ICE-6G_D.
Steffen21	Steffen (2021)	26 models representing the possible parameter space. Earth profiles include VM5a, VM7, and other 2-layer models (see Figure S1); ice history from ICE-6G_C, ICE-7G, and ANU-ICE (Peltier et al., 2018; Lambeck et al., 2014).
LM17.3	Steffen et al. (2021)	Earth profile from VM5a; ice history from multiple models.

Table 1: GIA models used in this study.

As a first-order approximation, we assume that uncertainties in the satellite data, steric corrections, and model outputs are independent of each other. Therefore, the total uncertainty in the ocean mass budget closure is calculated using the standard error propagation formula.

3.2 GIA-Corrected Degree-1 Coefficients

Since GRACE does not measure the degree-1 geopotential coefficients, the solutions provided in TN-13 are estimated from GIA-corrected higher degree coefficients by solving the SLE (Sun, Ditmar, & Riva, 2016; Sun, Riva, & Ditmar, 2016). That is, for each GIA model, there is a corresponding set of estimated degree-1 coefficients. Using a different model correction, while still substituting TN-13's coefficients based on the ICE-6G model, may lead to inconsistencies and complications when interpreting the mass budget closure (see Horwath et al., 2022).

We rederive the degree-1 coefficients following the approach described in TN-13 (Sun, Riva, & Ditmar, 2016), and the SLE is solved at d/o 180 using the procedure described in Section 2.3. More details of the rederivation are provided in the Supporting Information. When using their preferred ICE-6G model and optimal setup, we find that our degree-1 coefficients are consistent with the values reported in TN-13, validating our rederivations. A side-by-side comparison of the degree-1 coefficients from the TN and our reestimation with the same conditions (Figure S2) shows the closest agreement.

3.3 Signal Localisation

We project GRACE and subsequently derived data from the real spherical harmonic space onto a basis of scalar spherical Slepian functions to perform our analysis. As spherical harmonics lose orthogonality on a partial sphere, analysing regional phenomena with them is more challenging and prone to contamination from signals and noise outside the domain of interest.

Scalar Slepian basis functions are linear recombinations of spherical harmonics basis that optimally concentrate signal power in the domain of interest, both spatially and spectrally. Additionally, they are orthogonal both globally and locally (Simons et al., 2006, which also provides a more comprehensive review for interested readers), therefore requiring fewer basis functions to represent a signal in the domain of interest. These properties make Slepian functions more suitable for analysing regional signals, especially when the signal is weak and the noise is strong (Harig & Simons, 2012). Slepian functions have been used to study many regional phenomena, including mass change in regions as small as Iceland (von Hippel & Harig, 2019).

Briefly, Slepian basis functions, g, concentrate their power as solutions to the eigenvalue problem

$$\sum_{\ell'=0}^{L} \sum_{m'=-\ell'}^{\ell'} D_{\ell m,\ell' m'} g_{\ell' m'} = \lambda g_{\ell m}, \tag{10}$$

where the eigenvalue λ is the fraction of the total energy of the signal in the domain of interest. We truncate the basis when λ becomes low (as indicated by the Shannon number Simons et al., 2006), using only functions with the most concentrated energy. The kernel matrix, $\mathbf{D}$, is defined as the inner products of real spherical harmonics over the region of interest R as

$$D_{\ell m,\ell' m'} = \int_R Y_{\ell m} Y_{\ell' m'}\, d\Omega\,. \tag{11}$$

Figure 2 shows four of the Slepian functions from an example Slepian basis constructed over the global ocean with a 2° buffer at a bandwidth of $L = 20$.

3.4 Additional Processing

It is a known issue that the definition of the ocean domain and other processing choices can significantly affect the retrieved mass change (e.g. Han et al., 2019; Jeon, 2021). In this study, we first apply a 10° circular buffer around the epicentre of two coastal megathrust earthquakes (the 2004 Sumatra and 2011 Tohoku earthquakes) to filter out most tectonic deformation signals.

Second, the choice of the land-sea buffer, the maximum spherical harmonic degree, and the filtering also affect the recovered degree-1 coefficients and the mass change. The appropriate values are found through grid search synthetic experiments, as described in Harig & Simons (2012) and von Hippel & Harig (2019): A synthetic signal is constructed over the land, and the buffer width around the coastline and the maximum spherical har-

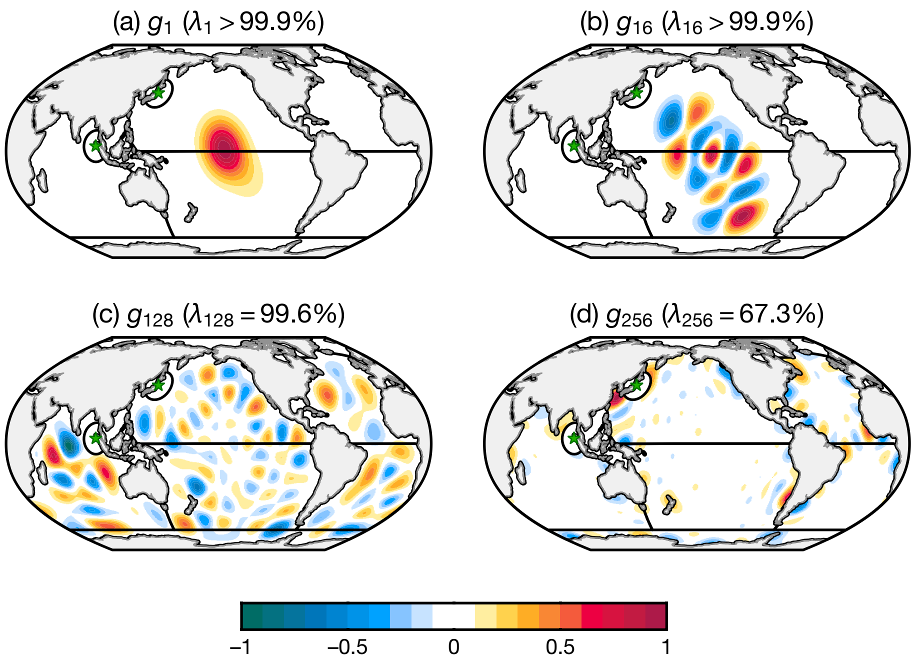

Figure 2: Four normalised functions from an example Slepian basis constructed at spherical harmonics degree $L = 20$ over the global ocean with a 2° buffer along the coastline (boundary shown in black). The Shannon number N is 251.9.

monics degree are varied until there is minimal leakage of the land signal into the ocean domain. As demonstrated in Figure S3, at the native GRACE resolution of d/o 60, a 0.5° buffer is sufficient to remove most of the land signal leakage into the ocean. Hence, we apply a 0.5° buffer to all processing in this study, and no additional filtering or scaling of the GRACE data is applied to minimise signal distortion.

It is for this reason that we deviate our setup from the preferred choice of GRACE TN-13 (Sun, Riva, & Ditmar, 2016), which has GRACE data truncated to d/o 45 and used a 200 km buffer. Whilst the bandwidth does not significantly affect the magnitude of the retrieved signal (provided it is sufficiently large; see Figure S3), the buffer size does. While we can faithfully reproduce the degree-1 coefficients in TN-13 using their setup, when C_{20} and C_{30} are additionally included in the inversion process, the seasonal variations of Sun, Riva, & Ditmar (2016) are exaggerated compared to the SLR solutions in TN-14. With our setup, the root mean square errors between the inverted seasonal $\Delta C_{20}/\Delta C_{30}$ and the SLR measurements in TN-14 have been reduced by 20% and 14%, respectively, indicating a better self-consistency of the inverted degree-1 coefficients.

4 Results

4.1 Global Ocean Mass Change

The GIA-corrected global mean ocean mass change time series and trends are shown in Figure 3, and summarised in the first column of Table 2. The values are estimated from the ensemble of the GRACE products from the three data centres and represent the weighted mean and spread after the GIA correction is applied. In the ensemble, each data centre's product is given equal weight, and the GIA models are weighted as follows: The 26 Steffen21 models that represent possible scenarios are each given a weight of 1; models that have been used in past studies including Paulson07, A13, ICE-6G, and LM 17.3, are given a weight of 4; Caron18 and Caron19 are each given a weight of 2, for they have similar expressions in the ocean. During trend estimation, a degree-2 polynomial is used, and sub-annual cycles are removed by fitting and subtracting sinusoidal functions with annual, semi-annual, and 161-day periods (Peltier, 2009).

Globally, from January 2003 to December 2022, the GRACE ensemble ocean mass change rate estimated with the GIA-corrected degree-1 coefficients recomputed in this study is 2.25±0.48 mm/yr. This value is in good agreement with the fingerprint-based estimate of 2.20±0.42 mm/yr. Since the mass conservation constraint is applied in the SLE, the difference between the two estimates stems from the different ocean domains used in the SLE and the global mean ocean mass (GMOM) estimates, where the latter

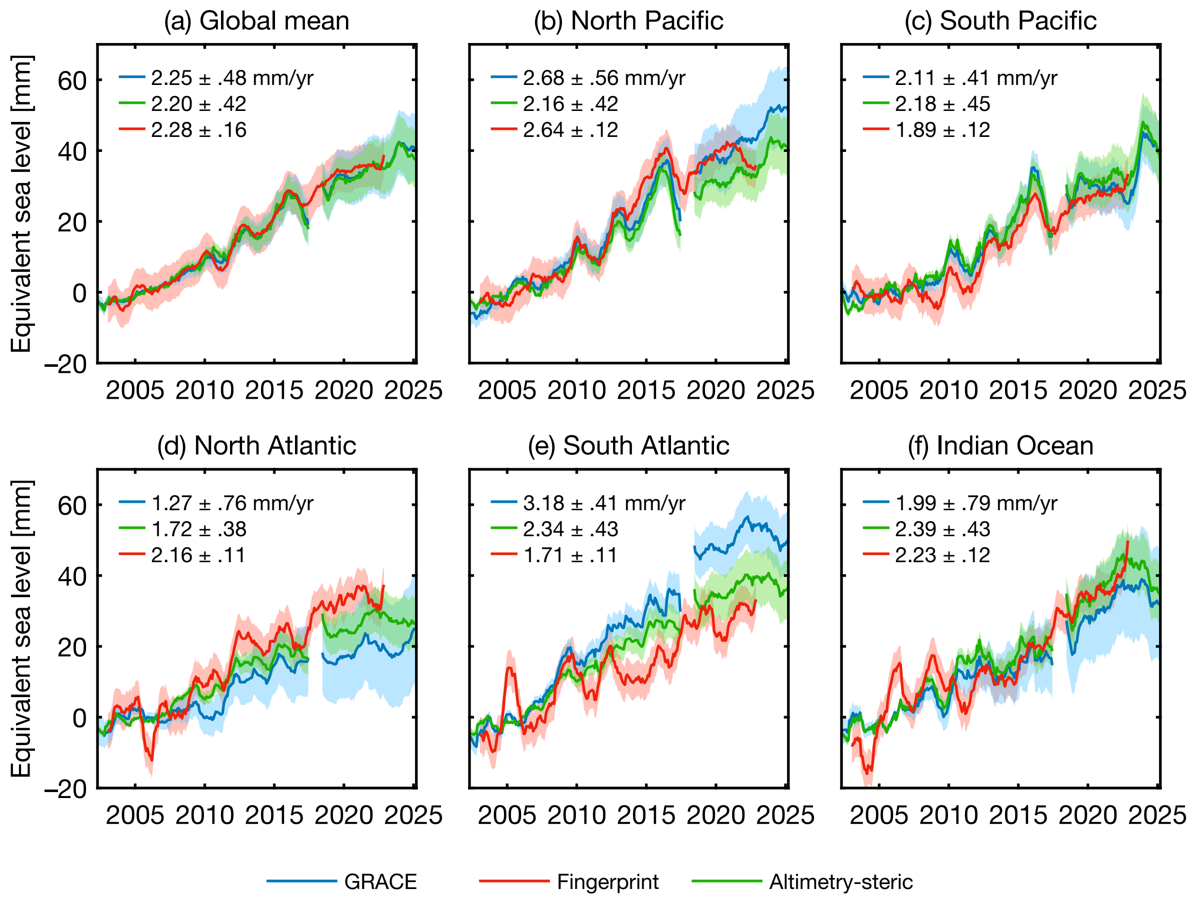

Figure 3: GIA-corrected ensemble mean estimates and spreads of ocean mass change (a) globally and (b–f) in each basin in terms of equivalent water thickness/sea level change, based on GAD-restored GRACE gravimetry (blue), GAD-added fingerprint (green), and steric-corrected altimetry (red). All estimates are created with re-estimated degree-1 coefficients. Seasonal signals are removed by applying a 1-year moving average filter. The changes are referenced to the mean ocean mass from 2003 to 2008, and the reported values are the linear trends from January 2003 to December 2022.

notably does not include the Arctic Ocean and some other small seas. Both estimates are consistent with the altimetry-steric estimate of 2.28±0.16 mm/yr within their uncertainties. In contrast, using separately two of the most up-to-date GIA models, ICE-6G and Caron19, with the TN-13 degree-1 coefficients yields 2.12 and 2.37 mm/yr, respectively. Either value falls within the ensemble's one-standard-deviation spread, but their difference is not negligible.

For the GRACE estimate, the uncertainty (the standard deiviation of the ensemble) at the global scale primarily comes from the different GIA model predictions (see Figures 4(a) and 5(a)), which is 0.4 mm/yr and overshadows the intrinsic uncertainties

Method	Geocentric motion	Ocean basins Global mean	N Pacific	S Pacific	N Atlantic	S Atlantic	Indian
GRACE	Reestimated	2.25 ± 0.48	2.66 ± 0.56	2.11 ± 0.41	1.27 ± 0.76	3.18 ± 0.41	1.99 ± 0.79
	TN-13	2.39 ± 0.42	2.65 ± 0.70	2.55 ± 0.38	1.05 ± 1.07	3.35 ± 0.49	1.97 ± 0.65
Fingerprint	Reestimated	2.20 ± 0.42	2.16 ± 0.42	2.18 ± 0.45	1.72 ± 0.38	2.34 ± 0.43	2.39 ± 0.43
	TN-13	2.30 ± 0.37	2.26 ± 0.38	2.28 ± 0.40	1.80 ± 0.36	2.45 ± 0.38	2.49 ± 0.38
Altimetry-steric		2.28 ± 0.16	2.64 ± 0.12	1.89 ± 0.12	2.16 ± 0.11	1.71 ± 0.11	2.23 ± 0.12

Table 2: The linear trend of the mass change in each ocean basin from January 2003 to December 2022.

of GRACE level-2 data (< 0.2 mm/yr) or the differences between data centres (< 0.1 mm/yr). The uncertainty in the fingerprint estimate is also dominated by the spread of GIA models, but from values on land instead of in the ocean. In general, models with a higher lower mantle viscosity lead to a faster global ocean mass increase (e.g. compare ICE-6G and Caron18/19 in Figures 5(a) and S1), as more seafloor/geoid depression has to be compensated by the ocean mass increase to match the satellite observations. Ocean dynamics (GAD) contribute negligibly to both methods' trends and their uncertainties.

The altimetry-steric global mass change rate has the smallest uncertainty among the three estimates. Since the effect of the GIA and OBD correction on the altimetry-steric measurements is small, the consequent mass change estimate has a much tighter spread envelope than the two GRACE-based estimates; in this case, GIA is not a significant source of uncertainty. All three estimates are consistent with each other and the values reported in Ludwigsen et al. (2024), especially after accounting for the spread of the GIA model predictions. Between 2007 and the decommission of GRACE in 2017, the three estimates also agree well with the interannual variability (Figure 3(a)). Beyond 2017, the GRACE and altimetry-steric estimates diverge slightly, which may be due to the salinity drift in the Argo data (Mu et al., 2024) and the removal of global mean halosteric sea level to account for it, but the decadal trends remain consistent.

When using the TN-13 degree-1 coefficients instead, the GRACE and fingerprint ensemble ocean mass change rate are slightly higher (Table 2), mainly because the ICE-6G_D model, paired with the TN13 setup (Sun, Riva, & Ditmar, 2016), results in a faster poleward (C_{10}) geocentric motion and hence a slower ocean mass increase (Figure 5(b)). Overall, the GIA-corrected degree-1 coefficients amplify the inter-model spread described in the previous passage, where models with high lower mantle viscosity bias towards degree-1 coefficients that predict a faster global ocean mass increase (see Figure 5(a)). Using the reestimated degree-1 coefficients slightly improves the agreement between the GRACE

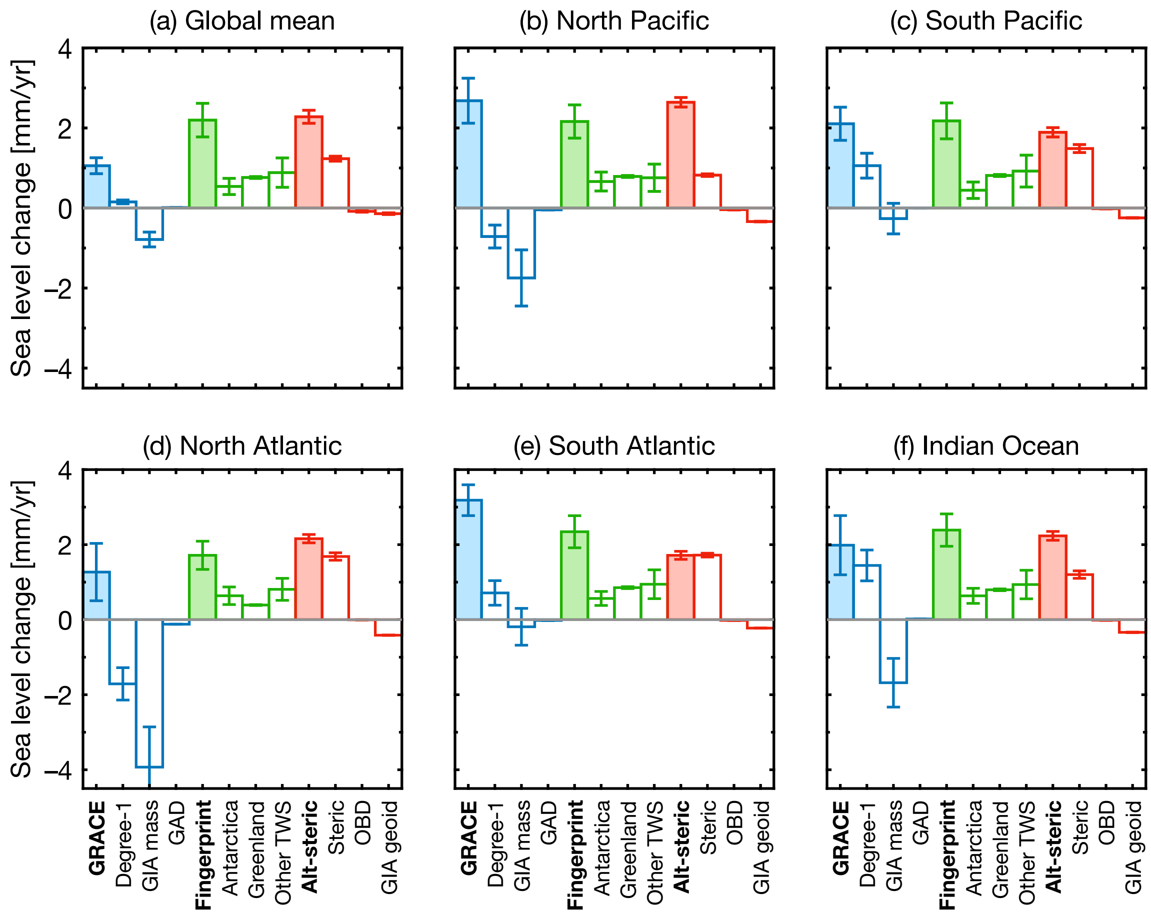

Figure 4: The contributions of different components to the basin mass budget trends from January 2003 to December 2022, in terms of equivalent water thickness/sea level change. The filled bars are the total ensemble trends, as in Figure 3.

and altimetry-steric estimates on this global scale. The uncertainty associated with the degree-1 coefficient is 0.13 mm/yr, which is consistent with the estimate from Horwath et al. (2022). For some individual models, the difference in the global ocean mass change rate can be above 0.2 mm/yr (10% of the total signal; Figure 5(a)). Still, the difference is not significant compared to the uncertainty from the GIA model spread (Figure 4(a)). The reestimated values also yield GMOM trends closer to ICE-6G_D forward model predictions that incorporate SLR data (M. Cheng, 2024), although the latter also has a considerable uncertainty from the data choice (2.09–2.24 mm/yr from 2002 to 2020). The direct SLR trends are also argued to be non-realistically low (Nie et al., 2025). The bottom line is that, at the global scale, our reestimation of the degree-1 coefficients shows that GIA has an additional downstream effect on the ocean mass change estimate via these coefficients. This represents an additional source of uncertainty whose magnitude

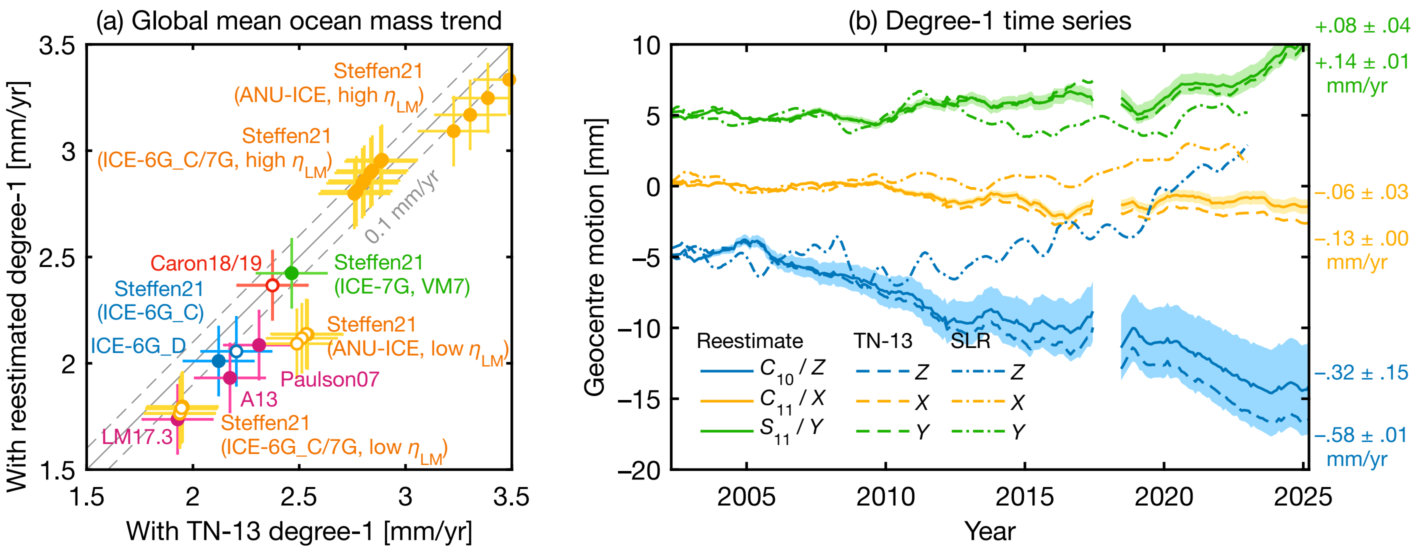

Figure 5: (a) GIA-corrected GRACE global ocean mass trends from 2002 to 2025, accounting for the GIA correction's effect on the degree-1 coefficients, compared to the trends derived using the Technical Note-13's degree-1 coefficients. The solid grey line is the line of identical trends from both the TN and our re-estimation, and the dashed grey line indicates a ± 0.1 mm/yr difference. (b) Comparison of the degree-1 coefficients (ΔC_{10}, ΔC_{11}, and ΔS_{11}) reestimated in this study using the ensemble of the GIA models (solid lines; patched area shows the 1σ inter-model spread) with those provided in Technical Note-13 (dashed lines). The seasonal signals are removed by applying a 1-year moving average filter. Also shown are the direct SLR measurements from M. Cheng (2024) for reference (dotted).

is comparable to other data choices that should be considered when interpreting the ocean mass change from GRACE data.

4.2 Basin-Scale Ocean Mass Change Estimates

The estimated mass change rates in individual ocean basins show more inconsistency than in the global case (Figure 3; Table 2). The GRACE basin-scale mass budgets and fingerprints inherit more uncertainties from the spread of the GIA model predictions than the global estimate (Figure 4). Hence, although in many basins, the differences between the three estimates are within the spread of GIA mode predictions, the basin-scale ocean mass budgets are not nearly as well-closed as the global budget.

In most basins, all three ensemble estimates yield inconsistent trends, regardless of whether the degree-1 coefficients are replaced. When we examine the spatial patterns of the difference between the two estimates (Figures 6 and S4), the Pacific Ocean shows the best agreement between the three estimates. In the North and South Pacific Oceans,

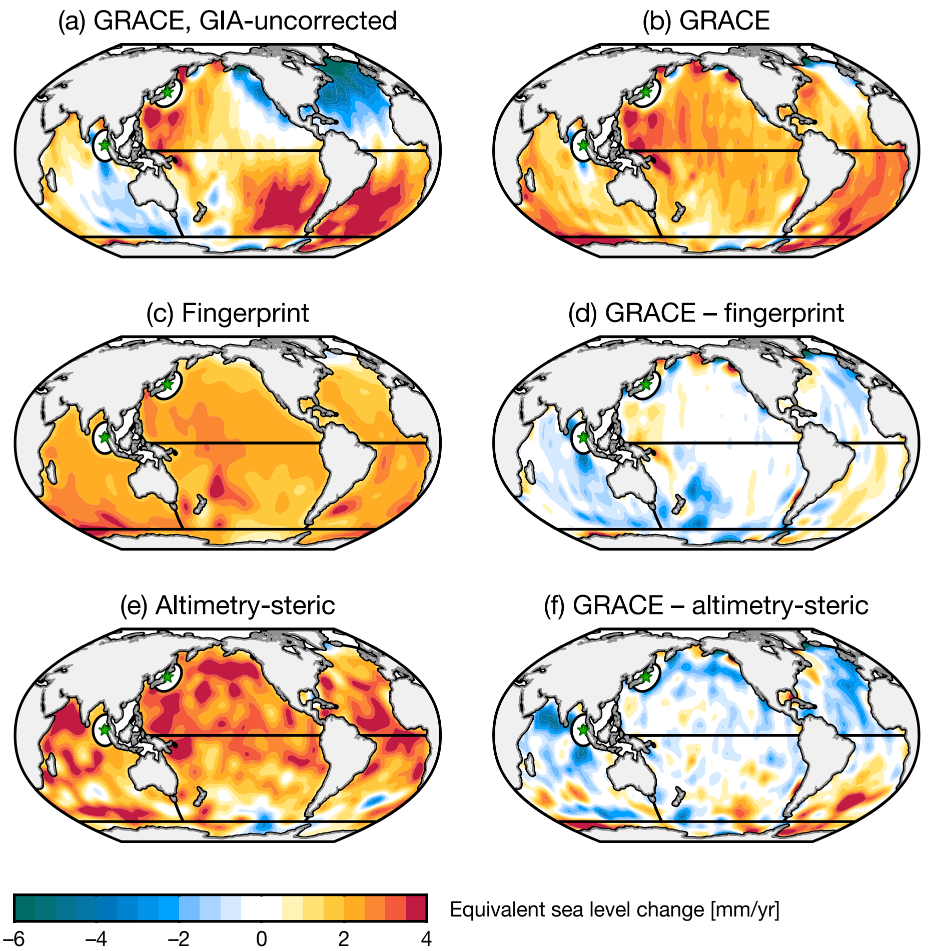

Figure 6: The spatial patterns of the ocean mass change rate ensemble estimations from GRACE data, the GRACE-derived fingerprint of the modern terrestrial water storage change, and the altimetry-steric measurements. The degree-1 coefficients are reestimated for individual GIA models, and GAD is restored for GRACE and the fingerprint to be comparable with the altimetry-steric fields. For visualisation purposes, a 400 km Gaussian filter is applied for $\ell \geq 20$.

the integrated mass change rates from the three estimates show reasonable agreement considering the range of GIA corrections (Figure 3(b) and (c)), but the spatial patterns suggest that this can be conincidental (Figures 6(d) and (f)), as there are still noticable differences at higher latitudes.

In the Indian Ocean, the discrepancies between the three estimates are more pronounced in two regions: the southwest of the 2004 Sumatra earthquake epicentre and the Arabian Sea. The former is likely due to residual co- and post-seismic deformation signals that are not fully removed by the 10° buffer around the epicentre. It can correspond to the sudden increase in altimetry-steric estimate around 2005 (Figure 3(d)), but its effect diminishes over time. In the latter region, the GRACE estimate is consistent with the fingerprint; hence, the discrepancy is more likely due to unmodelled OBD or steric effects in the altimetry-steric estimate. At the basin scale, the differences between the three estimates, while significant, are within the spread of the GIA model predictions.

As previously indicated (Mu et al., 2024), the Atlantic Ocean shows the largest discrepancies among the three estimates (Figure 3(e) and (f)), although the two basins exhibit different behaviours. In the North Atlantic Ocean, different GIA models predict a wide range of corrections due to the basin's proximity to the former Laurentide Ice Sheet. In the GRACE estimates, and to a lesser extent the fingerprint estimates, the uncertainty from the GIA model spread is so considerable that the results are not conclusive or suitable for detailed comparison with the altimetry-steric estimates.

Conversely, in the South Atlantic Ocean, the GIA correction is relatively minor and more consistent among models. Still, the three estimates differ significantly, with the fingerprint closer to the altimetry-steric estimate than to the GRACE estimate. This suggests that the discrepancies are likely from multiple sources, not solely the result of GIA correction. Notably, the altimetry-steric time series shows much more interannual variability than the other two estimates. Still, the difference could also indicate a systematic bias in the models in this basin.

Decomposing the spatial patterns into spherical harmonics (Figure 7) provides further insights into the source of the discrepancies. The difference between the GRACE and fingerprint estimates is dominated by the degree-2, order-1 coefficients, particularly C_{21}. Since C_{21} has a zero crossing in the middle of the Pacific Ocean (180°E/W), the Pacific basins show better agreement between the two estimates; the other zero crossing is near the boundary between the Indian and South Atlantic Ocean, and the difference between the two estimates has the opposite sign in these two basins (Figure 6(d)).

The spatial difference between the GRACE and altimetry-steric estimates also has a strong degree-2, order-1 component, but in addition has a strong degree-1 (C_{10}) component. The combination of these two components, which have the same sign in the Western Hemisphere, results in the pronounced North-South Atlantic dichotomy, with the GRACE estimates being lower in the North Atlantic and higher in the South Atlantic compared to the altimetry-steric estimates (Figure 6(f)). In this case, using the GIA-corrected degree-1 coefficients further pushes the GRACE estimates and fingerprints to be closer to the altimetry-steric measurements (Table 2).

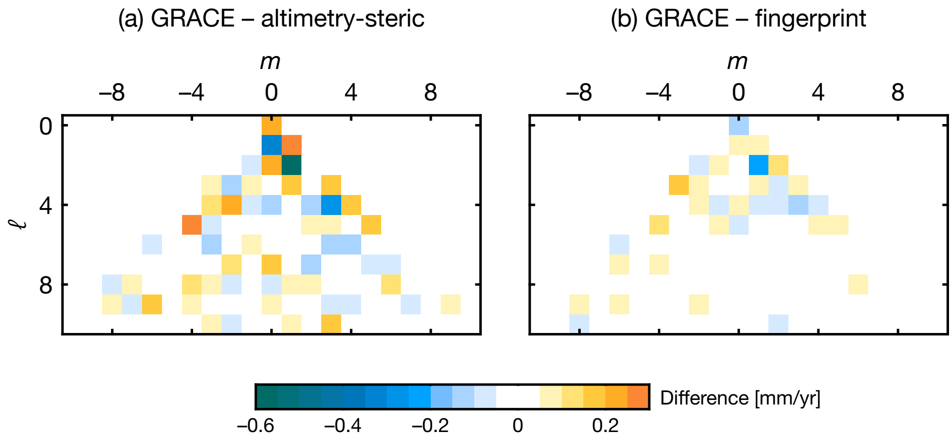

Figure 7: Spherical harmonic coefficient values of the difference between (a) the GRACE and altimetry-steric global mean ocean mass trend estimates in each basin, as shown in Figure 6(f). (b) is the same but for the difference between the GRACE estimate and fingerprint (Figure 6(d)). Note that the coefficients are for the ocean fields; therefore, the C_{00} difference is not zero. The spectrum has been truncated to d/o 10, and where positive orders ($m \geq 0$) correspond to the cosine terms ($C_{\ell m}$) and negative orders ($m < 0$) correspond to the sine terms ($S_{\ell|m|}$).

4.3 GIA Model Selection

In many basins, the differences between the three estimates are within or comparable to the spread of the GIA model predictions, suggesting that the choice of GIA model can significantly affect the basin-scale mass budget closure. This impact is clearly seen when we view the trend discrepancies for each basin and GIA model individually (Figure 8). The difference between the GRACE and fingerprint estimates is shown in the upper-left triangle, and the difference between the GRACE and altimetry-steric estimates is shown in the lower-right triangle. An entirely white square indicates agreement of all three estimates. No single model can close the mass budget in all basins simultaneously, and models exhibit a variety of behaviours across basins.

The ocean basins have varying sensitivity to the choice of GIA model. The South Pacific Ocean shows the most consistent mass change estimates among the three methods, for the most part, regardless of the GIA model used. In the basin, both the magnitude and the spread of the GIA correction are small relative to the other basins (Figure 4(c)), as it is farther from the LGM ice sheets and happens to be near the zero crossing of the rotational potential. The mass change estimates in the South Atlantic Ocean similarly do not depend strongly on the GIA model used, but the three estimates diverge significantly from each other regardless of the GIA model used. In contrast, the mass trends in the North Pacific, North Atlantic, and Indian Ocean depend heavily on the GIA model used. That is, whilst the ensemble estimates in these basins, especially the North Pacific Ocean, appear to be reasonably consistent between the three methods, the individual models show a wide range of behaviours.

Among the Steffen21 models, lower mantle viscosity appears to be a crucial factor in determining their ability to explain the non-closure of mass budgets in the sensitive basins (North Pacific, North Atlantic, and Indian). Their models with a relatively low lower mantle viscosity ($\eta_{\mathrm{LM}} = 2{\cdot}10^{21}\,\mathrm{Pa \cdot s}$) tend to cause the GRACE mass changes to under-predict the two other methods, especially in the Northern Hemisphere and the Indian Ocean. Models with a higher lower mantle viscosity ($20{\cdot}10^{21}\,\mathrm{Pa \cdot s}$) tend to cause the GRACE mass changes to over-predict the other estimates. The combination of the ice history and Earth model also matters, but to a lesser degree. Among the commonly used models, Caron18/19 appear to predict realistic degree-1 and 2 values despite having the highest lower mantle viscosity, and they perform best overall at closing mass budgets in most basins, except for the South Atlantic Ocean. This finding is coincident with the preference of Horwath et al. (2022). The ICE-6G_D model also performs reasonably well.

Corrections using the ANU-ICE model with a high mantle viscosity systematically predict significantly higher GRACE mass changes than the altimetry-steric values in all basins except for the North Atlantic Ocean. The difference implies that this combination of ice history and Earth model overcorrects the magnitude of the GIA effect in the ocean basins. We note that Lambeck et al. (2014) preferred an even higher lower mantle viscosity of $70{\cdot}10^{21}\,\mathrm{Pa \cdot s}$ out of the two possible solutions found in their study (the other one being $2 \cdot 10^{21}\,\mathrm{Pa \cdot s}$), which would lead to an even larger overcorrection.

In summary, directly and indirectly through the degree-1 coefficients, differences amongst GIA models can account for most of the non-closure global ocean mass budget. At the basin scale, they can explain nearly all of the discrepancies in the North and South Pacific and Indian Ocean mass budgets, roughly 60% of the non-closure in the North Atlantic Ocean, but only about 20% in the South Atlantic Ocean. The remaining discrepancies could represent unmodelled errors, but they could also indicate a systematic bias in the GIA models examined in this study, as the spatial patterns of the discrepancies correspond to specific spherical harmonic degrees and orders that are sensitive to GIA effects. The Steffen21 collection of models is not the most sophisticated nor realistic GIA models available, but they encompass a wide range of Earth structure and ice history scenarios from other studies and provide needed context to interpret the spatial dependence of sea level budget closure. Since no single model can simultaneously close mass budgets across all basins, systematic biases cannot be ruled out.

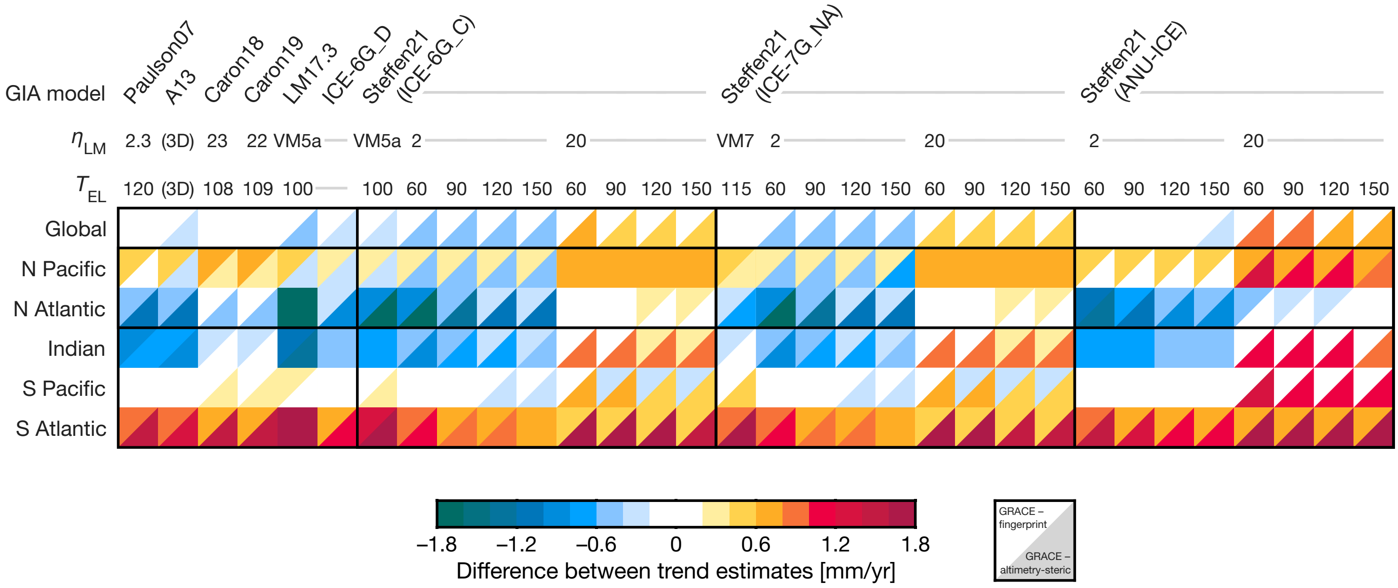

Figure 8: The difference between the ocean mass trends in each basin using the three methods and each of the GIA models. The upper-left triangle shows the difference between the GRACE estimates and the fingerprint, and the lower-right triangle shows the difference between the GRACE and the altimetry-steric estimates. GRACE and fingerprint estimates use reestimated degree-1 coefficients for each GIA model, and the GAD product is restored. The essential parameters of the GIA models are listed at the top; for more information, refer to Table 1 and Figure S1. T_{EL} [km]: elastic lithosphere thickness of the model; η_{LM} [10^{21} Pa s]: lower mantle viscosity.

5 Discussion

5.1 GIA Model Construction

The GIA models examined in this study are typically constructed by solving the self-consistent SLE for a compressible, one-dimensional, Maxwell solid Earth model, taking into account the topography and rotational feedback (except for A13, which employs a laterally varying Earth model; A et al. 2013). The underlying methodology for calculating the GIA response is similar to that of the fingerprint calculations described in Section 2.3 and the Supporting Information, but additionally involves convolution integrals over the ice loading and the viscous component of the Love numbers.

The ICE-6G model is one of the most widely used GIA models in GRACE applications in the ocean and beyond. It is the default model used in TN-13 and the construction of several mascon solutions. The ANU-ICE model is a popular alternative, often compared with the ICE-nG model or incorporated into composite models (Steffen et al., 2021; Caron et al., 2018; Pan et al., 2022). We consider the difference between them a good representation of the uncertainty in the GIA correction and also a helpful benchmark for model selection and direction for future model development. But since, for land applications, the long-wavelength predictions are not necessarily as important as the location of ice margins and near-field RSL predictions, they are not necessarily the best models for ocean applications. According to our results, for closing basin-scale ocean mass budgets, their performance varies across basins, and more suitable models likely exist.

The key observational constraints used in the models typically include coastal RSL records from the LGM to the present day and modern GNSS crustal motion measurements (e.g. Argus et al., 2014; Caron et al., 2018). Some models also use long-term GRACE data or glacial erratic exposure-age dating as additional constraints, to varying extents (e.g. Argus et al., 2014; Peltier et al., 2015). A major factor that differentiates the models is the spatial distribution of the RSL records used, which are by nature often sparse and unevenly distributed (Gale, 2023, Figure 6). The degree to which near-field (regions near the ancient ice margins) versus far-field RSL/GNSS records are used during model construction, therefore, contributes to the differences amongst models. For example, the ICE-nG series of models primarily utilises records from North America, Fennoscandia, and Antarctica (Peltier et al., 2015); meanwhile, the ANU-ICE model uses more equatorial coral records (Lambeck et al., 2014).

While the models are all 'global' models, they often focus on different regions or adopt composite ice models that perform well in specific regions but may be based on conditions or assumptions that are not globally applicable (LM17.3 is such an example of a composite model, Steffen et al. 2021; also Eicker et al. 2024). This varying focus leads to models potentially having greater fidelity in their areas or variables of interest, but potentially making unfavourable predictions in other regions, like the ocean basins.

The discrepancies between the models is, to some degree, a manifestation of the 'missing ice problem', which refers to the apparent 10–30 m discrepancy in eustatic sea level change since the LGM between far-field records and the modelled ice volume according to some ice history reconstructions (Gowan et al., 2021). Different GIA models prioritise different constraints when addressing this problem. Continuing from the previous example, the ANU-ICE model resolves the missing ice problem by allocating much more ice volume to Antarctica during the LGM compared to most other models; in contrast, the ICE-6G model accounts for a large proportion of global ice loss in the Northern Hemisphere but still shows a deficit relative to eustatic sea-level records (Gale, 2023). Furthermore, models with a high lower mantle viscosity imply slower relaxation of the GIA response to ice melting, thereby predicting higher present-day uplift and geoid deformation rates or requiring less ice volume or older deglaciation to match the same observations. These different model parameters demonstrate that a range of viscosity structures and ice distributions can provide a reasonable fit to the various observational data used as constraints, and the additional ocean mass budget closure criteria help further differentiate between models.

5.2 Long-Wavelength Ocean Mass Non-Closure

In the ocean, much energy of the GIA correction is concentrated in the degree-2, order-1 coefficients, as a result of the feedback on a rotating Earth (Milne & Mitrovica, 1998; Kendall et al., 2005). These coefficients produce the characteristic quadrupole pattern seen in the rate of geoid change (Figure 1). Additionally, we have shown that the estimated geocentric motion as represented by the degree-1 coefficients also depends strongly on the GIA model used (Figure 5(b)). These long-wavelength impacts of the GIA correction coincide with the dominant spatial patterns of the discrepancies between the three ocean mass change estimates (Figure 7); hence, these differences can be partially explained by the choice of the GIA model.

The degree-2, order-1 coefficients in the GRACE estimates are the most strongly affected by the GIA correction, where the magnitude of the effect is often comparable if not larger than the mass change signals in the ocean basins. Since the modern ocean mass change is much smaller than that of many ice sheets (e.g. Greenland and Antarctica), the accuracy of these coefficients impacts the GRACE direct ocean estimates more than the fingerprint estimates, which instead rely on the land signals. This spatial pattern then suggest that a sizeable portion of the differences between the three estimates in the Atlantic Ocean can be explained by unrealistic predictions of these coefficients in the GIA models. Our results indicate that the underestimation of C_{21} in many GIA models (Figure 7(a) and 5(a)) is a key factor in the non-closure of the basin-scale mass budgets, particularly in the Atlantic Ocean. This is unlikely to be explained by reference frame differences (Tamisiea, 2011), which would double C_{21} and S_{21}; this is too large compared to the discrepancies shown in Figure 7. The divergence between the GRACE and altimetry-steric estimates in the North and South Atlantic Ocean appears to be gradual (Figure 3), despite being obscured by interannual variability. We do not observe clear signals of sudden jumps in 2016 after removing the global mean halosteric sea level (Mu et al., 2024).

The C_{10} coefficient also plays a vital role in the north-south hemisphere partitioning of ocean mass change. Since the degree-1 terms vanish in the centre-of-mass frame that GRACE measures in, these coefficients are estimated with the higher-degree terms (Sun, Riva, & Ditmar, 2016). They are found by solving for the values that, when the land component is plugged into the SLE, the self-consistent solution is the ocean component. Hence, as the SLE is used, the estimates are sensitive to the GIA model used (see Figure 5(b)), and model selection therefore also plays a role in the north-south non-closure of ocean mass partitioning.

The difference between the GRACE and altimetry-steric estimates could be reconciled by a greater GIA response in the Northern Hemisphere, from a larger palaeo-ice volume, later deglaciation, or a much higher lower mantle viscosity. Replacing the TN-13 degree-1 coefficients with the ensemble reestimation, the differences between the C_{10} component of the GRACE and altimetry-steric estimates are reduced by 0.15 mm/yr. As the ANU-ICE models in the ensemble, which allocate more ice to Antarctica in the LGM, are less capable of closing mass budgets than the ICE-6G and 7G models, this corroborates the suggestion that ice history models with less ice in Antarctica are preferred. In fact, many Antarctica sutdies employ regional GIA models with even less ice in Antarctica during the LGM than ICE-6G (Harig & Simons, 2015; Ivins et al., 2013, and references therein).

The dependency of the basin-scale mass budget closure on the GIA model is less straightforward. Results from the Steffen21 models suggest that the ideal lower mantle viscosity is likely between 2 and $20{\cdot}10^{21}\,\mathrm{Pa\cdot s}$; VM5a and VM7 are such examples. Nonetheless, the Caron18/19 models, which both have high lower-mantle viscosity, predict favourable degree-1 and 2 GIA correction values and perform best overall at closing mass budgets in most basins, except for the South Atlantic Ocean. This likely reflects the fact that a wide range of trade-offs between viscosity profiles and ice history models can yield degree-1 and 2 GIA predictions that fit the observations similarly well (Caron et al., 2018). Our results further confirm this nuance: the LM17.3 model, which combines the VM5a profile with multiple state-of-the-art ice history models derived from different reconstructions, yields non-realistic predictions and performs very poorly at closing mass budgets in most basins.

5.3 Implications for Future GIA Model Construction

The closure of the basin-scale ocean mass budgets provides additional constraints on GIA models, especially the long-wavelength components that are most relevant to the ocean basins. This focus is different from what is typically prioritised in GIA model construction, which often emphasises fitting near-field RSL records and GNSS data. For the models examined in this study, we find that Caron18/19 predicts the most favourable long-wavelength GIA corrections for ocean mass budget closure. Still, this does not imply that the ice history and Earth model used in Caron18/19 are the most realistic overall or most appropriate for other applications, as different target variables are likely sensitive to different aspects of the models. Explicitly incorporating ocean mass budget closure in future GIA model development can improve the broader applications of these models.

From our degree-1 results, stronger GIA corrections in the Northern Hemisphere are preferred to close the basin-scale mass budgets. Combined with the degree-2, order-1 rotational signature of the LGM ice sheets, it is more straightforward to modify the Fennoscandian Ice Sheet than the Laurentide Ice Sheet to produce the desired spatial GIA pattern in the ocean. With a one-dimensional Earth model as most global GIA models use, this can be achieved by placing more ice in Fennoscandia during the LGM or delaying the onset of deglaciation.

RSL records from the near field of Fennoscandia used to construct global GIA models are sparse. The ANU-ICE and ICE-6G (which is not so different from ICE-5G, but with more ice load) models propose very different ice loads for the ice sheet from 25 to 15 ka in the region (Gale, 2023; Simon et al., 2018). The Fennoscandian maximum average ice thicknesses in both models are similar (230–240 m). Yet, the ice volume in the ICE-6G model steadily declines since 25 ka, while the ANU-ICE model did not reach maximum volume until 20 ka, followed by a more rapid deglaciation that ended before that of ICE-6G. The additional Fennoscandian ice, with less ice in Antarctica, in the ICE-6G-related models is consistent with their better performance in closing the ocean mass budgets. The spatial distribution of the ice load in Fennoscandia also differs between the two series of models. Caron18/19's Fennoscandian ice history is scaled from the ANU-ICE model, with an expected scale factor of 1.08 (Caron et al., 2018, this differs from the best-fit value of 0.89); the former is preferred to close mass budgets in most basins. Both the ANU-ICE and ICE-6G models fit the Peltier et al. (2015) Fennoscandian RSL data reasonably well over a wide range of Earth models (Gale, 2023), suggesting that the near-field RSL data in the region alone cannot distinguish between the two ice histories.

There exist regional Fennoscandian/Barents Sea models, notably the GLAC #71340 ice history and the subsequent NKG2016LU GIA model (Tarasov et al., 2014; Vestøl et al., 2019), which indeed place more ice in the Fennoscandian region than ICE-6G_D, and also have a later deglaciation onset (around 18 ka) that makes an ideal candidate for improving the ocean mass budget closure (Steffen et al., 2017). The model incorporates more modern GNSS data in the near field. Additionally, it is reportedly calibrated against the VM5a Earth model (Steffen et al., 2017), making it intercomparable with ICE-6G_D. Yet, we find that the LM17.3 model using the GLAC #71340 ice history and the VM5a viscosity profile performs poorly at closing ocean mass budgets in most basins.

This could merely indicate deficiencies in other regional models used in the LM17.3 construction, but the oceanic expressions of GLAC #71340 are otherwise not tested.

We therefore suggest that, for ocean applications, Fennoscandia is an ideal candidate region for adding more ice to future ice history models, with the additional benefit of partially alleviating the missing ice problem without significantly compromising the fit to the RSL records in other regions. This modification is also consistent with some suggestions from GNSS studies (Alvarez Rodriguez et al., 2025). This suggestion also implies that, the GIA models examined in this study, except for LM17.3, which has its own issues, have a systematic bias towards a higher GRACE-based ocean mass change rate in the South Atlantic Ocean. This bias is unaccounted for in the this study's ensemble uncertainties or values reported in other studies.

It is reasonable to assume that GIA corrections based on a laterally varying Earth model are necessary to fully resolve the ocean mass budget closure problem. Still, the baseline one-dimensional models have significant room for improvement, given the longer timespan and denser geodesy data available since their construction. State-of-the-art 3-D models (including the background 1-D viscosity profile, 3-D viscosity perturbations, lithosphere thickness variation, and more) are also subject to non-negligible uncertainties (Pan et al., 2022). Their impact on ocean mass budget closure remains to be explored, but the closure can similarly provide novel constraints for their development and validation. In the meantime, using an ensemble of GIA models and consistently applying them across all methods when assessing the ocean mass budgets is crucial to avoid biases and underestimation of uncertainties.

6 Conclusions

With the ensemble of 32 GIA models considered in this study, the GMOM change rates from January 2003 to December 2023 are 2.25 ± 0.48 mm/yr from GRACE data and 2.20 ± 0.42 mm/yr from the fingerprint method, both consistent with the altimetry-steric estimate of 2.28 ± 0.16 mm/yr. At the basin scale, the three estimates diverge more significantly in many basins. GIA model selection can explain most of the discrepancies in the Pacific and Indian Oceans, but only about 60% in the North Atlantic Ocean and 20% in the South Atlantic Ocean. Besides affecting the fingerprint and direct GRACE estimates, GIA's impact propagates into the OBD correction applied to the altimetry-steric measurements, further complicating the comparison between the two methods. Hence, using GIA models consistently across all methods is crucial when assessing the basin-scale mass budgets and their closure. Using the default TN-13 degree-1 gravimetry coefficients, which are based on the ICE-6G model, can lead to inconsistent basin-scale results across the three estimates compared with using the ensemble-reestimated degree-1 coefficients.

The first order of future business of closing the basin- and sub-basin-scale ocean mass budgets is to address the uncertainties in the long-wavelength components of the GIA correction. The inter-model spread of the spatial discrepancies amongst the GRACE and altimetry-steric measurements, and the fingerprint construction can largely be explained by the uncertainties in the C_{21}/S_{21} coefficients in the GIA models and how they affect the GRACE C_{10} estimates. These coefficients have different impacts across basins and, notably, constructively interfere in the North and South Atlantic Oceans, producing the largest discrepancies between the GRACE and altimetry-steric estimates.

Among the GIA models examined in this study, the Caron18/19 models are the most capable of closing the mass budgets in most basins, except for the South Atlantic Ocean, where all models suffer significant discrepancies. The ICE-6G_D (VM5a) model also performs reasonably well. Generally, the best-fitting lower mantle viscosity to the ICE-nG models falls between 2 and $20{\cdot}10^{21}$ $\mathrm{Pa}\cdot\mathrm{s}$; a lower value for the ANU-ICE model is preferred, but the model likely contains too much ice in Antarctica during the LGM to close the basin ocean mass budgets regardless. Nonetheless, our results still suggest that no single model can simultaneously close the mass budgets in all basins, and using a single model to correct for GIA can introduce significant biases in basin-scale mass estimates, leading to underestimation of their uncertainties and non-closure.

The closure of the basin-scale ocean mass budget thus provides another constraint for GIA model development. Our results suggest that models with less LGM ice load in Antarctica are preferred. Furthermore, the observed discrepancies could be partially resolved by a stronger GIA response in the Northern Hemisphere. Based on the spatial patterns, this is most straightforwardly achieved by placing more palaeo-ice load in the Fennoscandian Ice Sheet or delaying its deglaciation. This modification is consistent with some existing regional ice history models, and would not only improve ocean mass budget closure but also help alleviate the 'missing ice problem'.

Notations and Acronyms

Notations

h Sea surface height anomaly

n Geoid height anomaly

$\bar{n}$ A spatially uniform constant in the altimetric GIA correction

r Ocean bottom height anomaly

r^{GIA} GIA-induced vertical land motion

s Relative sea level

s^{SLF} Component of relative sea level due to the modern water redistribution from the land-ocean mass exchange. Also known as the sea-level fingerprint.

s^{dynamics} Component of relative sea level due to oceanic and atmospheric dynamics

s^{GIA} Component of relative sea level due to the viscoelastic response of the Earth due to past ice sheet deglaciation

s^{steric} Component of relative sea level due to steric effects

t Time

ϵ Unaccounted for changes in relative sea level, such as megathrust earthquakes

Ω Unit sphere

θ/ϕ Colatitude/longitude

ω Location on the unit sphere (in colatitude and longitude)

L Surface mass density load

M Total mass

ℓ/m Degree/order of spherical harmonics

f_ℓ^{E} Elastic load Love number for vertical displacement

k_ℓ^{E} Elastic load Love number for potential

$C_{\ell m}/S_{\ell m}$ Cosine/sine components of real spherical harmonics

$Y_{\ell m}$ General notation for real spherical harmonics, corresponding to $C_{\ell m}$ or $S_{\ell m}$ depending on the sign of m

Acronyms

GIA Glacial isostatic adjustment

GRACE Gravity Recovery and Climate Experiment

GFO GRACE Follow-On

LGM Last Glacial Maximum

OBD Ocean bottom deformation

RSL Relative sea level

SLE Sea level equation

SLF Sea level fingerprint

SLR Satellite laser ranging

TN (GRACE) Technical Note

Open Research Section

The A13 GIA model processed by NASA/JPL is available at https://podaac.jpl.nasa.gov/dataset/TELLUS_GIA_L3_0.5-DEG_V1.0; the Caron18/19 models are also available through NASA/JPL at https://vesl.jpl.nasa.gov/solid-earth/gia/. The Steffen21 and LM17.3 models are available from H. Steffen's personal website at https://sites.google.com/view/holgersteffenlm/startseite/data?authuser=0; the ICE-6G_D model is available from W. R. Peltier's personal webpage at https://www.atmosp.physics.utoronto.ca/~peltier/data.php.

All GRACE/GFO data used in this study are available from https://podaac.jpl.nasa.gov; the MEaSUREs gridded altimetry data is also available from PODAAC. The steric sea level is derived using the Gibbs-SeaWater (GSW) Oceanographic Toolbox (available at https://www.teos-10.org/software.htm) and data from the following sources: Data from the Argo Program were collected and made freely available by the International Argo Program and the national programs that contribute to it. (http://www.argo.ucsd.edu, http://argo.jcommops.org). The Argo Program is part of the Global Ocean Observing System. EN.4.2.2 data were obtained from https://www.metoffice.gov.uk/hadobs/en4/ and are l' British Crown Copyright, Met Office, 2025, provided under a Non-Commercial Government Licence http://www.nationalarchives.gov.uk/doc/non-commercial-government-licence/version/2/.

The code used to process the data and perform the analysis in this study is archived on Zenodo (Lee, 2025) or linked in the accompanying documentation. Main dependencies include the slepian_alpha and slepian_delta packages for spherical Slepian function analysis (Simons et al., 2020; Harig et al., 2024).

Conflict of Interest Disclosure

The authors declare there are no conflicts of interest for this manuscript.

Acknowledgments

The authors would like to thank M. Tamisiea for insightful discussions on GIA and ocean mass budget closure. This work was supported by the National Science Foundation (NSF) via Grant NSF-2142980, funded by the Geophysics programme, to C.H., and by the Gordon and Betty Moore Foundation through the Arizona's Science, Engineering, and Math Scholars (ASEMS) Scholar Training Academy for Research in STEM (STARS) programme to E.C.L.

References

A, G., Wahr, J., & Zhong, S. (2013, Feb). Computations of the viscoelastic response of a 3-D compressible Earth to surface loading: An application to glacial isostatic adjustment in Antarctica and Canada. *Geophysical Journal International*, *192*(2), 557–572. doi: 10.1093/gji/ggs030

Adhikari, S., Ivins, E. R., Frederikse, T., Landerer, F. W., & Caron, L. (2019, May). Sea-level fingerprints emergent from GRACE mission data. *Earth System Science Data*, *11*(2), 629–646. doi: 10.5194/essd-11-629-2019

Alvarez Rodriguez, G., Tregoning, P., & McGirr, R. (2025, Oct). A tool to assess the accuracy of glacial isostatic adjustment predictions of present-day crustal uplift rates. *Geophysical Research Letters*, *52*(20), e2025GL116421. doi: 10.1029/2025GL116421

Argus, D. F., Peltier, W. R., Drummond, R., & Moore, A. W. (2014, May). The Antarctica component of postglacial rebound model ICE-6G_C (VM5a) based on gps positioning, exposure age dating of ice thicknesses, and relative sea level histories. *Geophysical Journal International*, *198*(1), 537-563. doi: 10.1093/gji/ggu140

Caron, L., & Ivins, E. R. (2020, Feb). A baseline Antarctic GIA correction for space gravimetry. *Earth and Planetary Science Letters*, *531*, 115957. doi: 10.1016/j.epsl.2019.115957

Caron, L., Ivins, E. R., Larour, E., Adhikari, S., Nilsson, J., & Blewitt, G. (2018, Mar). GIA model statistics for GRACE hydrology, cryosphere, and ocean science. *Geophysical Research Letters*, *45*(5), 2203–2212. doi: 10.1002/2017GL076644

Chen, J., Tapley, B., Save, H., Tamisiea, M. E., Bettadpur, S., & Ries, J. (2018, Oct). Quantification of ocean mass change using Gravity Recovery and Climate Experiment, satellite altimeter, and Argo floats observations. *Journal of Geophysical Research: Solid Earth*, *123*(11), 10212–10225. doi: 10.1029/2018JB016095

Chen, J., Tapley, B. D., Seo, K.-W., Wilson, C., & Ries, J. (2019, Nov 20). Improved quantification of global mean ocean mass change using GRACE satellite gravimetry measurements. *Geophysical Research Letters*, *46*(23), 13984–13991. doi: 10.1029/2019GL085519

Cheng, L., Zhu, J., Cowley, R., Boyer, T., & Wijffels, S. (2014). Time, probe type, and temperature variable bias corrections to historical expendable bathythermograph observations. *Journal of Atmospheric and Oceanic Technology*, *31*(8), 1793–1825. doi: 10.1175/JTECH-D-13-00197.1

Cheng, M. (2024). An updated estimate of geocenter variation from analysis of SLR data. *Remote Sensing*, *16*(7). doi: 10.3390/rs16071189

Eicker, A., Schawohl, L., Middendorf, K., Bagge, M., Jensen, L., & Dobslaw, H. (2024, Apr). Influence of GIA uncertainty on climate model evaluation with GRACE/GRACE-FO satellite gravimetry data. *Journal of Geophysical Research: Solid Earth*, *129*(5), e2023JB027769. doi: 10.1029/2023JB027769

Fox-Kemper, B., Hewitt, H. T., Xiao, C., Aðalgeirsdóttir, G., Drijfhout, S. S., Edwards, T. L., … Yu, Y. (2021, Jun 29). Ocean, cryosphere and sea level change. In V. Masson-Delmotte et al. (Eds.), *Climate change 2021: The physical science basis: Working group I contribution to the sixth assessment report of the Intergovernmental Panel on Climate Change* (pp. 1211–1362). Cambridge, UK and NY, US: Cambridge University Press.

Gale, S. (2023, Apr). Investigating ANU and ICE-6G ice model relative sea level misfits to determine viscosity constraints since the Last Glacial Maximum. *University of Colorado Honors Journal*. doi: 10.33011/cuhj20242279

Gowan, E. J., Zhang, X., Khosravi, S., Rovere, A., Stocchi, P., Hughes, A. L. C., … Lohmann, G. (2021, Oct). A new global ice sheet reconstruction for the past 80 000 years. *Nature Communications*, *12*(1), 1199. doi: 10.1038/s41467-021-21469-w

Han, S.-C., Sauber, J., Pollitz, F., & Ray, R. (2019, Apr). Sea level rise in the Samoan Islands escalated by viscoelastic relaxation after the 2009 Samoa-Tonga earthquake. *Journal of Geophysical Research: Solid Earth*, *124*(4), 4142–4156. doi: 10.1029/2018JB017110

Harig, C. T., & Simons, F. J. (2012, Nov). Mapping Greenland's mass loss in space and time. *Proceedings of the National Academy of Sciences*, *109*(49), 19934–19937. doi: 10.1073/pnas.1206785109

Harig, C. T., & Simons, F. J. (2015, Feb). Accelerated West Antarctic ice mass loss continues to outpace East Antarctic gains. *Earth and Planetary Science Letters*, *415*(1), 134–141. doi: 10.1016/j.epsl.2015.01.029

Harig, C. T., Simons, F. J., von Hippel, M., Gourley, K. C., & Kettner, A. J. (2024). *slepian_delta* [Software]. GitHub/Zenodo. Retrieved from `https://github.com/csdms-contrib/slepian_delta` doi: 10.5281/zenodo.592812

Horwath, M., Gutknecht, B. D., Cazenave, A., Palanisamy, H. K., Marti, F., Marzeion, B., … Benveniste, J. (2022, Feb). Global sea-level budget and ocean-mass budget, with a focus on advanced data products and uncertainty characterisation. *Earth System Science Data*, *14*(2), 411–447. doi: 10.5194/essd-14-411-2022

Ivins, E. R., James, T. S., Wahr, J., O. Schrama, E. J., Landerer, F. W., & Simon,

K. M. (2013, May). Antarctic contribution to sea level rise observed by GRACE with improved GIA correction. *Journal of Geophysical Research: Solid Earth*, *118*(6), 3126–3141. doi: 10.1002/jgrb.50208

Jeon, T. (2021, Aug). Impact of ocean domain definition on sea level budget. *Remote Sensing*, *13*(16). doi: 10.3390/rs13163206

Jeon, T., Seo, K.-W., Kim, B.-H., Kim, J.-S., Chen, J., & Wilson, C. R. (2021, Aug). Sea level fingerprints and regional sea level change. *Earth and Planetary Science Letters*, *567*, 116985. doi: 10.1016/j.epsl.2021.116985

Jeon, T., Seo, K.-W., Youm, K., Chen, J., & Wilson, C. R. (2018, Sep 10). Global sea level change signatures observed by GRACE satellite gravimetry. *Scientific Reports*, *8*(1), 13519. doi: 10.1038/s41598-018-31972-8

Kendall, R. A., Mitrovica, J. X., & Milne, G. A. (2005, Oct). On post-glacial sea level–II. numerical formulation and comparative results on spherically symmetric models. *Geophysical Journal International*, *161*(3), 679–706. doi: 10.1111/j.1365-246X.2005.02553.x

Lambeck, K., Rouby, H., Purcell, A., Sun, Y., & Sambridge, M. (2014, Sep). Sea level and global ice volumes from the Last Glacial Maximum to the Holocene. *Proceedings of the National Academy of Sciences*, *111*(43), 15296–15303. doi: 10.1073/pnas.1411762111

Lee, E.-C. (2025). *Unified localisation of mass over oceans (ULMO)* [Software]. GitHub/Zenodo. Retrieved from `https://github.com/williameclee/ulmo` doi: 10.5281/zenodo.17625699

Loomis, B. D., Rachlin, K. E., Wiese, D. N., Landerer, F. W., & Luthcke, S. B. (2020, Jan). Replacing GRACE/GRACE-FO with satellite laser ranging: Impacts on Antarctic ice sheet mass change. *Geophysical Research Letters*, *47*(3), e2019GL085488. doi: 10.1029/2019GL085488

Ludwigsen, C. B., Andersen, O. B., Marzeion, B., Malles, J.-H., Hannes, M. S., Döll, P., … King, M. A. (2024, Feb). Global and regional ocean mass budget closure since 2003. *Nature Communications*, *15*(1), 1416. doi: 10.1038/s41467-024-45726-w

McDougall, T. J., & Barker, P. M. (2011). Getting started with TEOS-10 and the Gibbs Seawater (GSW) Oceanographic Toolbox [Computer software manual].

Milne, G. A., & Mitrovica, J. X. (1998, Apr). Postglacial sea-level change on a rotating Earth. *Geophysical Journal International*, *133*(1), 1–19. doi: 10.1046/j.1365-246X.1998.1331455.x

Mu, D., Church, J. A., King, M., Ludwigsen, C. B., & Xu, T. (2024, Aug). Contrasting discrepancy in the sea level budget between the North and South Atlantic Ocean since 2016. *Earth and Space Science*, *11*(8), e2023EA003133. doi: 10.1029/2023EA003133

Mu, D., Ludwigsen, C. B., Peng, F., Yan, H., & Xu, T. (2025, Oct). Modeling sea level rise over 1993–2022: Implications for understanding coastal observations. *Geophysical Research Letters*, *52*(20), e2025GL117434. doi: 10.1029/2025GL117434

Nie, Y., Chen, J., Peng, D., & Li, J. (2025). Inferring long-term geocenter motion from low-degree gravity field. *Journal of Geophysical Research: Solid Earth*, *130*(8), e2024JB030327. doi: 10.1029/2024JB030327

Pan, L., Milne, G. A., Latychev, K., Goldberg, S. L., Austermann, J., Hoggard, M. J., & Mitrovica, J. X. (2022, Aug). The influence of lateral Earth structure on inferences of global ice volume during the Last Glacial Maximum. *Quaternary Science Reviews*, *290*, 107644. doi: 10.1016/j.quascirev.2022.107644

Paulson, A., Zhong, S., & Wahr, J. (2007, Nov). Inference of mantle viscosity from GRACE and relative sea level data. *Geophysical Journal International*, *171*(2), 497–508. doi: 10.1111/j.1365-246X.2007.03556.x

Peltier, W. R. (2009, Aug). Closure of the budget of global sea level rise over the GRACE era: The importance and magnitudes of the required corrections for global glacial isostatic adjustment. *Quaternary Science Reviews*, *28*(17), 1658–1674. doi: 10.1016/j.quascirev.2009.04.004

Peltier, W. R., Argus, D. F., & Drummond, R. (2015, Nov). Space geodesy constrains ice age terminal deglaciation: The global ICE-6G_C (VM5a) model. *Journal of Geophysical Research: Solid Earth*, *120*(1), 450–487. doi: 10.1002/2014JB011176

Peltier, W. R., Argus, D. F., & Drummond, R. (2018, Nov 23). Comment on "An assessment of the ICE-6G_C (VM5a) glacial isostatic adjustment model" by Purcell et al. *Journal of Geophysical Research: Solid Earth*, *123*(2), 2019–2028. doi: 10.1002/2016JB013844

Peltier, W. R., Wu, P. P.-C., Argus, D. F., Li, T., & Velay-Vitow, J. (2022, Sep). Glacial isostatic adjustment: physical models and observational constraints. *Reports on Progress in Physics*, *85*(9), 096801. Retrieved from `https://dx.doi.org/10.1088/1361-6633/ac805b` doi: 10.1088/1361-6633/ac805b

Rietbroek, R., Brunnabend, S.-E., Kusche, J., Schröter, J., & Dahle, C. (2016, Jan 25). Revisiting the contemporary sea-level budget on global and regional scales. *Proceedings of the National Academy of Sciences*, *113*(6), 1504–1509. doi: 10.1073/pnas.1519132113

Roemmich, D., & Gilson, J. (2009, Aug). The 2004–2008 mean and annual cycle of temperature, salinity, and steric height in the global ocean from the Argo Program. *Progress in Oceanography*, *82*(2), 81–100. doi: 10.1016/j.pocean.2009.03.004

Shepherd, A., Ivins, E., Rignot, E., Smith, B., van den Broeke, M., Velicogna, I., … The IMBIE Team (2019, Dec). Mass balance of the Greenland Ice Sheet from 1992 to 2018. *Nature*, *579*(7798), 233–239. doi: 10.1038/s41586-019-1855-2

Simms, A. R., Lisiecki, L., Gebbie, G., Whitehouse, P. L., & Clark, J. F. (2019, Feb). Balancing the last glacial maximum (LGM) sea-level budget. *Quaternary Science Reviews*, *205*, 143-153. Retrieved from `https://www.sciencedirect.com/science/article/pii/S0277379118304074` doi: 10.1016/j.quascirev.2018.12.018

Simon, K. M., Riva, R. E. M., Kleinherenbrink, M., & Frederikse, T. (2018, Jun). The glacial isostatic adjustment signal at present day in northern Europe and the British Isles estimated from geodetic observations and geophysical models. *Solid Earth*, *9*(3), 777–795. doi: 10.5194/se-9-777-2018

Simons, F. J., Dahlen, F. A., & Wieczorek, M. A. (2006). Spatiospectral concentration on a sphere. *SIAM Review*, *48*(3), 504–536. doi: 10.1137/S0036144504445765

Simons, F. J., Harig, C. T., Plattner, A., & von Hippel, M. (2020). *slepian_alpha* [Software]. GitHub/Zenodo. Retrieved from `https://github.com/csdms-contrib/slepian_alpha` doi: 10.5281/zenodo.15704

Spada, G. (2017, Jan). Glacial isostatic adjustment and contemporary sea level rise: An overview. *Surveys in Geophysics*, *38*(1), 153–185. doi: 10.1007/s10712-016-9379-x

Steffen, H. (2021, Oct). *Surface deformations from glacial isostatic adjustment models with laterally homogeneous, compressible Earth structure* [Dataset]. doi: 10.5281/zenodo.5560862

Steffen, H., Gowan, E., Ivins, E., Lecavalier, B., Milne, G., Purcell, A., … Wu, P. (2017). Task 3.8 – GIA (correction) for hydrology status January 2017. In *EGSIEM general assembly 8-9 June 2017.* DLR Oberphaffenhofen, Germany. Retrieved from `https://egsiem.eu/images/static/GA_Bern_Jan2017/Annex09_WP3_GIA_Status.pdf`

Steffen, H., Li, T., Wu, P., Gowan, E. J., Ivins, E., Lecavalier, B., … Whitehouse, P. L. (2021). *LM17.3 - a global vertical land motion model of glacial isostatic adjustment* [Dataset]. PANGAEA. doi: 10.1594/PANGAEA.932462

Sun, Y., Ditmar, P., & Riva, R. E. M. (2016, Jan). Observed changes in the

Earth's dynamic oblateness from GRACE data and geophysical models. *Journal of Geodesy*, *90*(1), 81–89. Retrieved from `https://doi.org/10.1007/s00190-015-0852-y` doi: 10.1007/s00190-015-0852-y

Sun, Y., Riva, R., & Ditmar, P. (2016, Nov). Optimizing estimates of annual variations and trends in geocenter motion and j_2 from a combination of GRACE data and geophysical models. *Journal of Geophysical Research: Solid Earth*, *121*(11), 8352–8370. doi: 10.1002/2016JB013073

Tamisiea, M. E. (2011, Sep). Ongoing glacial isostatic contributions to observations of sea level change. *Geophysical Journal International*, *186*(3), 1036–1044. doi: 10.1111/j.1365-246X.2011.05116.x

Tarasov, L., Hughes, A. L. C., Gyllencreutz, R., Lohne, Ø. S., Mangerud, J., & Svendsen, J.-I. (2014). The global GLAC-1c deglaciation chronology, melwater pulse 1-a, and a question of missing ice. In *IGS symposium on contribution of glaciers and ice sheets to sea-level change, IGS symposium abstracts.*

Uebbing, B., Kusche, J., Rietbroek, R., & Landerer, F. W. (2019, Feb). Processing choices affect ocean mass estimates from GRACE. *Journal of Geophysical Research: Oceans*, *124*(2), 1029–1044. doi: 10.1029/2018JC014341

Vestøl, O., Ågren, J., Steffen, H., Kierulf, H., & Tarasov, L. (2019, Sep). NKG2016LU: a new land uplift model for Fennoscandia and the Baltic Region. *Journal of Geodesy*, *93*(9), 1759–1779. doi: 10.1007/s00190-019-01280-8

Vishwakarma, B. D., Royston, S., Riva, R. E. M., Westaway, R. M., & Bamber, J. L. (2020, Jan). Sea level budgets should account for ocean bottom deformation. *Geophysical Research Letters*, *47*(3), e2019GL086492. doi: 10.1029/2019GL086492

von Hippel, M., & Harig, C. T. (2019, Jul 04). Long-term and inter-annual mass changes in the Iceland ice cap determined from GRACE gravity using Slepian functions. *Frontiers in Earth Science*, *7*, 171. doi: 10.3389/feart.2019.00171

Wahr, J., Molenaar, M., & Bryan, F. (1998, Dec). Time variability of the Earth's gravity field: Hydrological and oceanic effects and their possible detection using GRACE. *Journal of Geophysical Research: Solid Earth*, *103*(B12), 30205–30229. doi: 10.1029/98JB02844

WCRP Global Sea Level Budget Group. (2018, Aug). Global sea-level budget 1993–present. *Earth System Science Data*, *10*(3), 1551–1590. doi: 10.5194/essd-10-1551-2018

Supporting Information for 'The Impact of GIA Corrections on Gravimetric Basin-Scale Ocean Mass Budgets'

En-Chi Lee[1,2] and Christopher Harig[1]

[1]Department of Geosciences, University of Arizona

[2]Lunar and Planetary Laboratory, University of Arizona

Contents of this file

1. Text S1 and S2, with a list of notations

2. Figures S1 to S4

Introduction: Text S1 and S2 provides more detailed derivations of the sea level equation (SLE) and its use in estimating the degree-1 coefficients from Gravity Recovery and Climate Experiment (GRACE) data, respectively. Supporting figures 1–4 provide additional validation of the processing steps and results presented in the main text, including the robustness of the degree-1 coefficient estimation, synthetic tests of signal leakage, and extra trend maps using GRACE Technical Note (TN)-13 degree-1 coefficients. Also included is a figure showing the viscosity profiles of the glacial isostatic adjustment (GIA) models used in this study.

Text S1, The Sea Level Equation: The relative sea level (RSL) s is defined as the difference between the sea surface height (i.e. the geoid perturbation plus a spatially uniform constant) and the solid Earth surface height, also known as ocean bottom deformation (OBD) or vertical land motion (VLM). Here we briefly summarise the SLE used in this study to solve for the surface load L given land water and ice mass changes from GRACE data. The formulation below closely follows that of Adhikari, Ivins, Frederikse, Landerer, and Caron (2019). In the full SLE, it can be expressed in the spherical harmonic domain as the sum of elastic and viscous responses, and the spatially uniform offset term (Spada, 2017; Adhikari et al., 2019):

$$s_{\ell m}(t) = s^{\mathrm{E}}_{\ell m}(t) + s^{\mathrm{V}}_{\ell m}(t) + z(t)\delta_{\ell 0}\delta_{m0}, \tag{S1}$$

with the elastic component expressed as

$$s^{\mathrm{E}}_{\ell m}(t) = \frac{3}{\rho_\oplus}\frac{1 + k^{\mathrm{E}}_\ell - f^{\mathrm{E}}_\ell}{2\ell+1} L_{\ell m}(t) + (1 + k'^{\mathrm{E}}_\ell - f'^{\mathrm{E}}_\ell)\frac{\Lambda_{\ell m}(t)}{g_0}, \tag{S2a}$$

and the viscous component expressed as

$$s^{\mathrm{V}}_{\ell m}(t) = \int_{t_0}^{t} \left(\frac{3}{\rho_\oplus}\frac{k^{\mathrm{V}}_\ell(t-t') - f^{\mathrm{V}}_\ell(t-t')}{2\ell+1} L_{\ell m}(t') + \left(k'^{\mathrm{V}}_\ell(t-t') - f'^{\mathrm{V}}_\ell(t-t')\right)\frac{\Lambda_{\ell m}(t')}{g_0}\right) \mathrm{d}t' \,. \tag{S2b}$$

Similar to Equation (8) of the main text, the spatially constant term is given by the conservation of global water mass:

$$\int_{\mathrm{ocean}} \left(\sum_{\ell,m} \left(s^{\mathrm{E}}_{\ell m} + s^{\mathrm{V}}_{\ell m}\right) Y_{\ell m} + z\right) \mathrm{d}\Omega = -\int_{\mathrm{land}} \left(\sum_{\ell,m} F_{\ell m} Y_{\ell m}\right) \mathrm{d}\Omega, \tag{S2c}$$

where F is the land forcing, which in this study comes from the GIA-corrected GRACE measurements. The total load is then the sum of land forcing and the relative sea level change over the ocean:

$$L = F + O(\rho_{\mathrm{w}} s), \tag{S3}$$

with O being the ocean function (1 in ocean, 0 on land) and ρ_w the density of water.

In the equations above, k_ℓ and f_ℓ are the load Love numbers (LLNs) describing the geoid and VLM's gravitational responses to surface loading, respectively; their difference is therefore the relative sea level response, as described above. The primed versions (k'_ℓ and f'_ℓ) are the tidal Love numbers (TLNs), which describe the rotational potential response instead. For both versions, the superscripts 'E' and 'V' denote the elastic and viscous components, respectively.

The surface load L is the sum of surface mass changes from ice, land water, and ocean mass redistribution. The rotational potential Λ is a function of the load as well as the Earth's inertia tensor (see Adhikari et al., 2019).

The elastic term, Equation (S2a), represents the instantaneous response of the solid Earth to surface loading changes, that is, the sea-level fingerprint (SLF) of modern water redistribution. The convolution viscous term, Equation (S2b), represents the effect of GIA on sea level, which, in GIA models, is commonly reported term-wise as geoid deformation and VLM. Because of the exponential decay of the viscous response, setting the lower bound of the integral (t_0) to the Last Glacial Maximums (LGMs) is a sufficient approximation for present-day sea-level change.

Taking the integral of a function (say, u) over the ocean, as seen in Equation (S2c), is identical to taking integral over the entire globe, but instead of the original function multiplied by the ocean function, with the property

$$(Ou)_{\ell m} = \sum_{\ell' m'} D_{\ell m, \ell' m'} u_{\ell' m'}, \tag{S4}$$

The kernel matrix $\mathbf{D}$ is defined in Equation (11) of the main text, with the ocean being the region of interest. The formulation above allows us to leverage the orthogonality of spherical harmonics to solve for the spatial constant z:

$$z = -\frac{1}{\rho_{\mathrm{w}}}\frac{F_{00}}{O_{00}} - \frac{(Os^{\mathrm{E}})_{00} + (Os^{\mathrm{V}})_{00}}{O_{00}}. \tag{S5}$$

Thus, all terms in the SLE are expressed in the spherical harmonic domain, allowing us to solve for the load L iteratively.

Text S2, GRACE Degree-1 Coefficients: The estimation of geocentric motion with GRACE data, as in e.g. Sun, Riva, and Ditmar (2016) or this study, exploits Equation (S4). More generally, when a coefficient of the load is unknown (say, $L_{\ell m}$), Equation (S4) can be expanded as

$$(OL)_{\ell m} = D_{\ell m,\ell m}L_{\ell m} + \sum_{\ell' m'}(D_{\ell m,\ell' m'}L_{\ell' m'})(1 - \delta_{(\ell m)(\ell' m')}), \tag{S6}$$

where the first term on the right-hand side contains the unknown coefficient, and the second term contains all other known coefficients. Equation (S6) is equivalent to Equations (3)–(5) of Sun et al. (2016). The unknown coefficient can then be estimated using the SLE as described above, and iteratively refined until Equation (S6) is satisfied.

Equation (S6) can also be easily adapted to estimate multiple unknown coefficients simultaneously. In this study, we are primarily interested in estimating the degree-1 coefficients (L_{10} and $L_{1\pm1}$), which can be converted back to the Stokes coefficients C_{10}, C_{11}, and S_{11} for comparison with GRACE TN-13.

The coefficients now estimated with satellite laser ranging (SLR), C_{20} and C_{30}, can also be estimated in the same manner. Ideally, these estimated coefficients should be consistent with the SLR measurements. We indeed use this metric as one of the arguments for the robustness of our degree-1 estimation, with a setup that differs from Sun et al. (2016), but a more detailed investigation is outside the primary scope of this study.

Notations: On top of the notations listed in the main text, we also use the following notations in the supporting information:

δ_{ij} Kronecker delta function

g_0 Reference gravitational acceleration at the Earth's surface

$\rho_\oplus$ Bulk density of the Earth

ρ_w Density of water

$k_\ell^\mathrm{E}/k_\ell^\mathrm{V}$ Elastic/viscous component of load Love number (LLN) for geoid response

$k_\ell'^\mathrm{E}/k_\ell'^\mathrm{V}$ Elastic/viscous component of tidal Love number (TLN) for geoid response

$f_\ell^\mathrm{E}/f_\ell^\mathrm{V}$ Elastic/viscous component of LLN for vertical land motion (VLM) response

$f_\ell'^\mathrm{E}/f_\ell'^\mathrm{V}$ Elastic/viscous component of TLN for VLM response

Λ Rotational potential

F Terrestrial forcing load for the sea level equation (SLE)

O Ocean function

$\mathbf{D}$ Kernel matrix of the ocean function

References

Adhikari, S., Ivins, E. R., Frederikse, T., Landerer, F. W., & Caron, L. (2019, May). Sea-level fingerprints emergent from GRACE mission data. *Earth System Science Data*, *11*(2), 629–646. doi: 10.5194/essd-11-629-2019

Caron, L., & Ivins, E. R. (2020, Feb). A baseline Antarctic GIA correction for space gravimetry. *Earth and Planetary Science Letters*, *531*, 115957. doi: 10.1016/j.epsl.2019.115957

Caron, L., Ivins, E. R., Larour, E., Adhikari, S., Nilsson, J., & Blewitt, G. (2018, Mar). GIA model statistics for GRACE hydrology, cryosphere, and ocean science. *Geophysical Research Letters*, *45*(5), 2203–2212. doi: 10.1002/2017GL076644

Peltier, W. R., Argus, D. F., & Drummond, R. (2018, Nov 23). Comment on "An assessment of the ICE-6G_C (VM5a) glacial isostatic adjustment model" by Purcell et al. *Journal of Geophysical Research: Solid Earth*, *123*(2), 2019–2028. doi: 10.1002/2016JB013844

Roy, K., & Peltier, W. R. (2018). Relative sea level in the Western Mediterranean basin: A regional test of the ICE-7G_NA (VM7) model and a constraint on late Holocene Antarctic deglaciation. *Quaternary Science Reviews*, *183*, 76-87. doi: 10.1016/j.quascirev.2017.12.021

Spada, G. (2017, Jan). Glacial isostatic adjustment and contemporary sea level rise: An overview. *Surveys in Geophysics*, *38*(1), 153–185. doi: 10.1007/s10712-016-9379-x

Steffen, H. (2021, Oct). *Surface deformations from glacial isostatic adjustment models with laterally homogeneous, compressible Earth structure* [Dataset]. doi: 10.5281/zenodo.5560862

Steffen, H., Li, T., Wu, P., Gowan, E. J., Ivins, E., Lecavalier, B., … Whitehouse, P. L. (2021). *LM17.3 - a global vertical land motion model of glacial isostatic adjustment* [Dataset]. PANGAEA. doi: 10.1594/PANGAEA.932462

Sun, Y., Riva, R., & Ditmar, P. (2016, Nov). Optimizing estimates of annual variations and trends in geocenter motion and j_2 from a combination of GRACE data and geophysical models. *Journal of Geophysical Research: Solid Earth*, *121*(11), 8352–8370. doi: 10.1002/2016JB013073

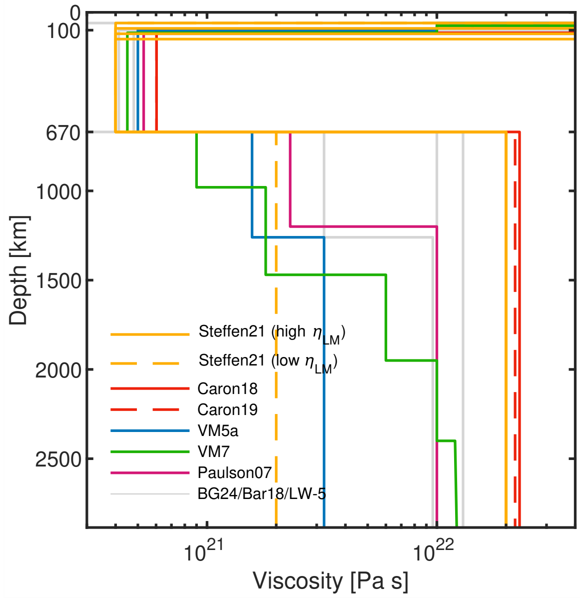

Figure S1. Viscosity profiles of the GIA models used in this study (Caron et al., 2018; Caron & Ivins, 2020; Peltier et al., 2018; Roy & Peltier, 2018; Steffen, 2021; Steffen et al., 2021) and some additional viscosity models for comparison.

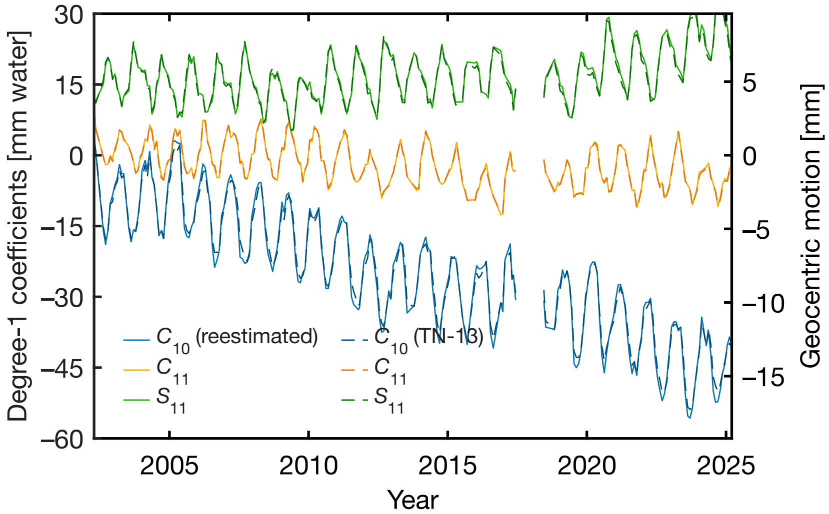

Figure S2. Degree-1 coefficients as reported in TN-13 and our rederivation with a similar setup (2° buffer, GAD-corrected GRACE data up to degree 45 with no filtering, solving the SLE; cf. Sun et al., 2016).

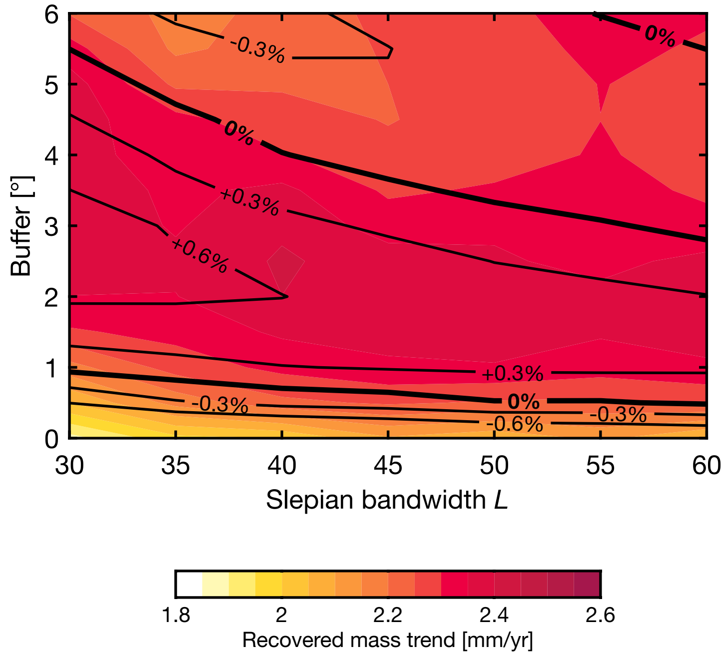

Figure S3. The recovered GRACE global mean ocean mass trend from January 2003 to December 2022 using Slepian functions constructed with different land-sea buffers and maximum spherical harmonics degrees L. The overlaid contours indicate the percentage of synthetic terrestrial signal leakage into the ocean domain, as a fraction of the original signal amplitude on land.

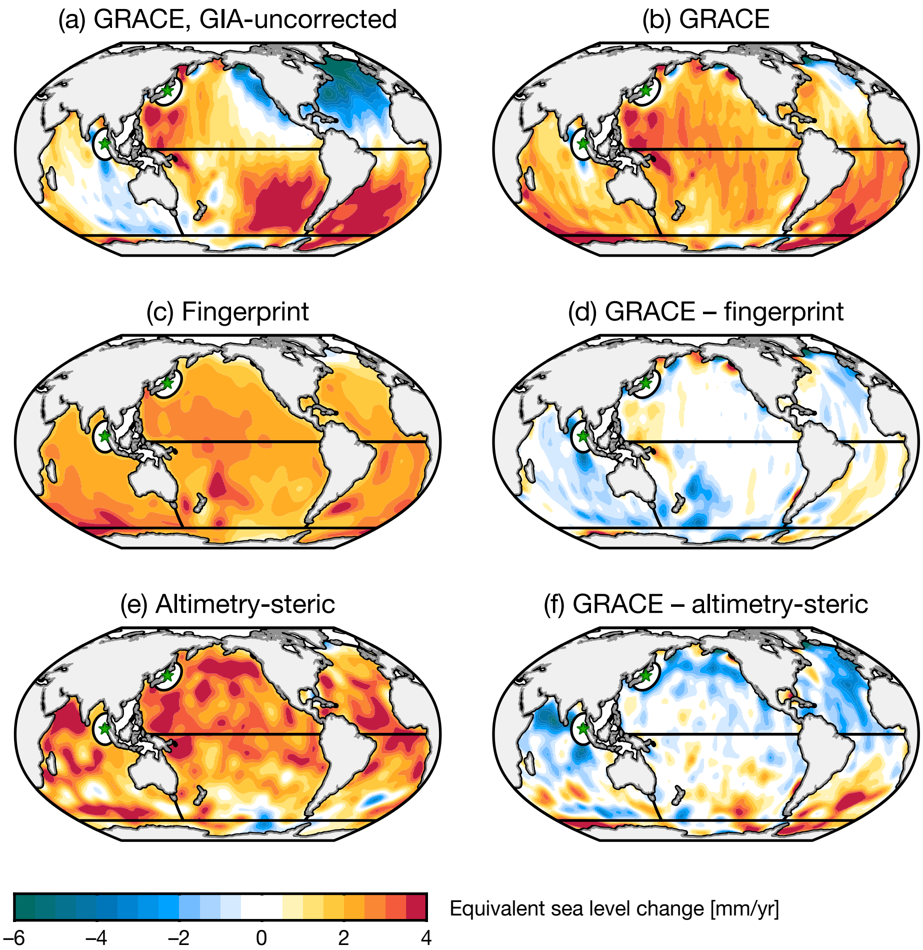

Figure S4. Same as Figure 6, but the degree-1 coefficients are from TN-13 and not reestimated.